Revision of 4815R1

Atomistic simulation on mixing thermodynamics of calcite-smithsonite solid solutions

Xin Liu, Xiancai Lu*, Xiandong Liu, Huiqun Zhou

State Key Laboratory for Mineral Deposit Research, School of Earth Sciences and Engineering, Nanjing University, Nanjing Jiangsu, 210026, China

Running title: *Thermodynamics of $Zn_xCa_{1-x}CO_3$ calcites*

* Corresponding author.

Email: xcljun@nju.edu.cn

Tel: +86 25 89681065

Fax: +86 25 89680703

ABSTRACT

By using atomistic simulation and configurational statistics techniques, the thermodynamics of mixing for calcite-smithsonite solid solutions have been investigated. By employing a 2 × 2 × 1 supercell, the configuration with the lowest energy for the solid solution with a certain composition was determined. The incorporated Zn^{2+} tends to occur at the sites neighboring to another substituted Zn^{2+} within the (0001) layer, but the substituted layers are preferentially segregated by calcite layers, and vice versa. The supercells with compositions around the two end members stand positive enthalpies at any temperatures, whereas those supercells with composition of about $Ca_{0.5}Zn_{0.5}CO_3$ prominently exhibit negative values in various temperatures of reality (e.g. <1000 K). The free energies are prominently negative at high temperatures (>1500 K) for the whole range of compositions, only those around both end members have positive values at some low temperatures (<1200 K). In the derived phase relations of this solid solution system, the potential incorporation content of $ZnCO_3$ into calcite is only 0-2.5% mole fraction (i.e. Zn content of 0-1.6 wt%) in most geochemistry equilibrium processes, and vice versa.

Keywords: calcite-smithsonite, solid solution, mixing thermodynamics, atomistic simulation

INTRODUCTION

Calcite can incorporate many divalent cations (e.g. Zn^{2+}, Mn^{2+}, Cd^{2+}, Fe^{2+}, Sr^{2+}, and Mg^{2+}) at the Ca^{2+} positions due to their similar ionic radii and bonding properties (Hume-Rothery et al. 1969), thus there are a series of solid solutions with calcite structure in nature. Calcite and its isomorphs are important in many fields, such as geo-sequestration of carbon dioxide (Herzog 2001; Bickle 2009; Matter and Kelemen 2009), nuclear waste repository (Curti 1999; Curti et al. 2005; Zavarin et al. 2005), bio-mineralization (Sarret et al. 2007; Isaure et al. 2010), and so on. The calcite-structured solid solution with substitution of Zn^{2+} is commonly found in weathering or oxidized products of Zn-bearing rocks or zinc ores (Boni et al. 2007; Coppola et al. 2008; Balassone et al. 2008; Boni et al. 2009; Mondillo et al. 2011). Smithsonite is the end member of fully Zn-substituted calcite, and its crystallographic parameters are similar to those of calcite. As new sphalerite mines are becoming more difficult to find, new processes are being developed to produce Zn metal from oxidized Zn ores, which have long been an important alternative source of Zn after sulfides (Zhao and Stanforth, 2000; Espiari et al., 2006; Navidi Kashani and Rashchi, 2008; Irannajad et al., 2009; Mehdilo et al., 2013) and have been found in carbonate forms in different parts of the world, such as China, Iran, Yemen, Peru, and so on (Boni et al., 2007; Feng et al., 2007; Balassone et al., 2008; Coppola et al., 2008; Boni et al., 2009; Chen et al., 2009; Li et al., 2010; Shi et al., 2012; Shi et al., 2013).

The substitution of Zn into calcite have been studied experimentally and

55 theoretically. But the content of substituted Zn in calcite is thought as limited, and
56 vice versa, due to approximately 26% difference of ionic radii between Zn^{2+} (0.74 Å)
57 and Ca^{2+} (1.00 Å) (Shannon 1976). Crocket and Winchester (1966) experimentally
58 studied the coprecipitation of Zn with calcium carbonate and found that smithsonite is
59 less soluble than calcite or aragonite, and trace Zn in geofluids tends to be
60 coprecipitated with calcium carbonate in nature. Based on their experimental data and
61 a binary regular solid solution model, Glynn and Reardon (1990) found the free
62 energy of mixing (ΔG_M) is negative across the whole range and further determined a
63 symmetric miscibility gap between $Ca_{0.8}Zn_{0.2}CO_3$ and $Ca_{0.2}Zn_{0.8}CO_3$. In fact, the
64 maximum incorporation of Zn into calcite are considerately low from both natural and
65 synthesized samples (Reeder 1983). Natural calcite with a Zn content higher than
66 1wt% has seldom been reported yet. Reeder and his colleagues measured five
67 Zn-bearing synthesized and natural calcite, and found the Zn content ranges from 245
68 to 1200 ppm (Lamble et al. 1997; Reeder et al. 1999). Temmam et al. (2000) reported
69 two samples of calcite from coprecipitation experiments, one has a Zn content no
70 more than 2000 ppm and the other is Zn-rich with a maximum incorporation up to 1.4
71 wt% which had been considered as a separate phase and affected by the incorporation
72 of Mn. However, the bio-mineralized calcites can accommodate high substituted Zn.
73 For example, calcite precipitation with extremely high contents of Zn up to 7.71 wt%
74 and Mn was found in a bacteria mediated tufa deposition on the wall of a subsurface
75 lane in a Pb-Zn mine by electron microprobe analysis (EMPA) (Liu et al. 2009).

Sarret et al. (2007) also found calcites with high Zn contents up to 8.22 wt% in tobacco leaves. There are also a few reports on the incorporation of Ca^{2+} into smithsonite with a maximum content of 1.04 wt% and some extreme high values up to 8.5 wt% accompanied by a high contents of Fe (Boni et al. 2007; Balassone et al. 2008; Coppola et al. 2008; Boni et al. 2009). In fact, by using common instrumental measurements like EMPA, the measured content of an impurity element does not always represent the incorporation into the lattice of a certain solid solution mineral because there are sometimes "invisible" nanosized mineral inclusions, narrow zonations, nanotextured exsolusions, intergrowths in natural samples generally extending well below the spot size of the electron probe beam (Cook et al. 2009, 2011; Ciobanu et al. 2011)..

At present, rapid development of molecular simulation has made it a promising alternative strategy to experimental methods for investigation of physical-chemical properties of substitutions in minerals at the atomic level (Vinograd and Sluiter 2006; Vinograd et al. 2006b; Vinograd et al. 2007b; Vinograd et al. 2008; Vinograd et al. 2007c). For thermodynamic studies of solid solution, employment of molecular simulation can avoid the effects of unknown kinetic factors. By using interatomic potential models, the mixing energy and substitution behaviors of calcite-structured solid solutions have been studied (Vinograd et al. 2006a, 2007a, 2009; Wang and de Leeuw 2008; Wang et al. 2011). By integrating with the previously proposed "cluster expansion" method (Connolly and Williams 1983; Sanchez et al. 1984), the excess

97 mixing properties of alloys can be accurately predicted from atomistic level. In this
98 method, the energy of each configuration of a specific supercell can be calculated
99 from each pairwise interactions energy, *J* (Becker et al. 2000; Reich and Becker 2006;
100 Ferriss et al. 2010; Renock and Becker 2011). For the calculation of *J*, Vinograd et al.
101 (2009) proposed a double-defect method (DDM), which have shown high
102 performance (Jung et al. 2010; Kulik et al. 2010; Vinograd et al. 2010a, 2010b;
103 Vinograd and Winkler 2010). The *J*s calculation is conducive to predict the most
104 stable configuration of a supercell. In recent years, by using a configurational
105 statistics method developed by Grau-Crespo et al. (2004, 2007), the most
106 thermodynamically stable configuration as well as other thermodynamic properties
107 can be obtained (Wang and de Leeuw 2008; Ruiz-Hernandez et al. 2010; Grau-Crespo
108 et al. 2011; Wang et al. 2011; Haider et al. 2012). This method is based on the
109 calculation of all inequivalent site occupancy configurations in a relevant small
110 supercell. However, because there are actually substantive inequivalent configurations
111 in a large supercell the computational cost of this method will dramatically increase
112 for a relatively lager supercell. So, a series of supercells with different sizes should be
113 tested for the convergence and computational cost with respect to supercell size.
114 In this study, the thermodynamics of mixings in calcite-smithsonite solid solution
115 were calculated by using both DDM and configurational statistics methods. A series
116 of substituted 2 × 2 × 1, 3 × 3 × 1, and 4 × 4 × 1 supercells of calcite/smithsonite with
117 24, 54, and 96 replaceable cation sites were considered, respectively. Thermodynamic

properties, such as enthalpy, entropy, and free energy of mixing, were obtained. Then, 11 *J*s respectively for calcite and smithsonite were calculated by employing DDM and a 3 × 3 × 1 supercell. Thus, the most stable configurations with a certain composition can be obtained and explained by combining the entropy of mixing with *J*s. Finally, we derived phase relations from free energy isotherms with common tangent analysis, from which we can estimate the maximum content of substituted cation in calcite-smithsonite solid solution at a specific temperature.

METHODS

Force field

This study used the interatomic potentials (Table 1) developed for carbonate minerals (Rohl et al. 2003; Austen et al. 2005), which accurately reproduce the cell parameters, elastic constants and bulk moduli in simulations of phase relations of the rhombohedral carbonates solid solutions (Vinograd et al. 2007a, 2009, 2010b). Based on the Born model of solids (Born et al. 1954), this force field considers two kinds of interactions between ions, i.e. long-rang interactions by electrostatic forces and short-rang interactions. The short-rang van der Waals interactions are described by a Buckingham potential. Two-, three-, and four-body potentials are used to model the covalent interactions within a CO_3^{2-} group, which are in forms of Morse potential, three-body angular potential, and out-of-plane potential, respectively. The electronic polarizability of oxygen in CO_3^{2-} is modeled via a core-shell model (Dick Jr and Overhauser 1958), in which each polarizable ion has a core and a massless shell,

connected by a spring potential. The program GULP (Gale 1997, 2005; Gale and Rohl 2003) were used for static lattice energy calculations.

The cell parameters and bulk moduli of calcite and smithsonite calculated with the selected force field are listed in Table 2. Compared with the experimental data (Dandekar and Ruoff 1968; Graf 1961; Zhang and Reeder 1999), the deviation is mostly below 1.2% except bulk modulus of calcite, which is overestimated by 5.6% also within a reasonable range.

Supercells

Considering a certain composition of a supercell including numbers of conventional hexagonal unit cells, Ca^{2+} and Zn^{2+} ions can be arranged in various ways, and thus the supercell presents a large number of configurations. By using a SOD (site occupancy disorder) program developed by Grau-Crespo et al. (2007), the symmetrically inequivalent configurations of solid solution with a certain composition can be extracted by a set of symmetry operators of the parent structure. Assuming zero external pressure and ignoring vibrational contributions because of its little contributions (Benny et al. 2009; Ruiz-Hernandez et al. 2010; Wang et al. 2011), static lattice energy of each symmetrically inequivalent configuration was obtained through geometry optimizations with GULP package. In the optimizations, we carried out constant pressure energy minimization calculations, in which both the cell parameters and ion positions are allowed to vary.

In this study, we considered cation substitutions in 2 × 2 × 1, 3 × 3 × 1, and 4 × 4 ×

1 supercells of calcite/smithsonite with 24, 54, and 96 replaceable cation sites, respectively. Because the *c* of the cell is big enough to exclude the interactions between the cations in neighboring cells, we only extended the *a*, *b* axes to 2 or 3 times of themselves. With SOD program, the reduced configurational space of calcite-smithsonite solid solutions with different substitution was derived and presented in Table 3. For the 3 × 3 × 1 and 4 × 4 × 1 supercells, the configurations for highly substituted compositions of $Zn_xCa_{1-x}CO_3$ were not calculated due to the expensive computational cost. According to the reported composition of calcite-smithsonite solid solutions, $0.093 < x < 0.907$ of 3 × 3 × 1 supercells, $0.042<x<0.958$ of 4 × 4 × 1 supercells were not considered here.

Configurational statistics

The static lattice energies of all symmetrically inequivalent configurations calculated by using GULP can be presented as a configurational energetic spectrum for a certain composition. Since the configurations of lower energy are more stable thermodynamically for a particular composition, the probabilities of occurrence for each single configuration are weighted by a Boltzmann factor $\exp(-E/k_BT)$ (k_B is Boltzmann's constant) for a given temperature T (Yeomans 1992). From the lattice energy E_m (m=1,…, M, M is the number of inequivalent configurations) calculated by GULP and the configuration degeneracy Ω_m (characterizing the occurred times of each inequivalent configuration in the complete configurational space), we can obtain the probability of occurrence (Grau-Crespo et al. 2004, 2007; Wang et al. 2011):

$$P_m = \frac{\Omega_m}{Z}\exp(-E_m / k_B T) \qquad \text{Eq.1}$$

where Z is the configurational partition function:

$$Z = \sum_{m=0}^{M} \Omega_m \exp(-E_m / k_B T) \qquad \text{Eq.2}$$

The configurational free energy G per formula unit at each composition can be obtained directly from the partition function:

$$G = -\frac{1}{N} k_B T \ln Z \qquad \text{Eq.3}$$

where N is the number of formula units in a supercell. Since we have assumed zero external pressure and have ignored vibrational contributions to the energy, the enthalpy is simply the energy of each configuration (E_m). Then the enthalpy for each composition can be estimated from configurational space averaging:

$$H = \frac{1}{N}\sum_{m=1}^{M} P_m H_m = \frac{1}{N}\sum_{m=1}^{M} P_m E_m \qquad \text{Eq.4}$$

Any average observable A for each composition, e.g. cell parameters, can be obtained by the same course:

$$A = \sum_{m=1}^{M} P_m A_m \qquad \text{Eq.5}$$

Then the entropy S can be calculated from the enthalpy and free energy:

$$S = \frac{H - G}{T} \qquad \text{Eq.6}$$

It has been confirmed that the convergence of free energy and entropy of solid solution supercells is much slower than enthalpy (Todorov et al. 2004; Wang et al. 2011). In this study, we employed three sizes of supercells to test the convergence and found that a 2 × 2 × 1 supercell is sufficient to ensure adequate convergence in all

compositions for enthalpy, but is not large enough for free energy and entropy. Therefore, the entropies here are only used to discuss the degree of disorder of substitution in solid solutions. The difference between the fully disordered entropy of a given supercell with a particular composition [$S_{max}(x,N)$] and the ideal fully disordered entropy of a continuous lattice with same composition [$S_{ideal}(x)$] can be used to assess the degree of convergence of entropies with the size of the supercell. Both entropies can be calculated by the follow functions:

$$S_{max}(x,N) = \frac{1}{N} k_B \ln \frac{N!}{[Nx]![N(1-x)]!} \qquad \text{Eq.7}$$

$$S_{ideal}(x) = \lim_{N\to\infty} S_{max}(x,N) = -k_B[x\ln x + (1-x)\ln(1-x)] \qquad \text{Eq.8}$$

RESULTS AND DISCUSSION

Energy spectra and probability distribution of configurations

For each supercell with different composition, the inequivalent configurations were calculated and listed in Table 3. The static lattice energy of each inequivalent configuration was calculated and summarized in an energy spectra. All the compositions have very wide configurational spectra except only 1 substitution in a supercell due to the only inequivalent configuration. For example, Fig. 1 shows the static lattice energy spectra and the distribution of all the configurations with the composition of $Ca_{0.5}Zn_{0.5}CO_3$ in a 2 × 2 × 1 supercell, where all the energies have subtracted the lowest-energy. The maximum energy difference between different supercell configurations of $Ca_{0.5}Zn_{0.5}CO_3$ is approximately 413 kJ/mol (Fig. 1). It is

clear that there are enormous numbers of configurations with energy of 200 kJ/mol < E < 360 kJ/mol after considering the degeneracy. As taking the Boltzmann factor into account, the lowest-energy configuration contribute the highest weight and the others even can be ignored at low temperatures, but at higher temperatures (normally >800 K) its contribution decreases while others' contribution increases (Fig. 2).

Entropy and the most stable configurations

Configurational entropy is a quantitative parameter used to measure the degree of ion ordering. Fig. 3a shows the variation of the maximum entropy (Eq. 7, high temperature limit) with respect to different supercell sizes. The dash line represents the configurational entropy of an ideal fully disordered system, i.e. the fully disordered entropy with respect to an infinite supercell (Eq. 8). The configurational entropy is not converged well for all used supercells with various sizes (2 × 2 × 1, 3 × 3 × 1 and 4 × 4 × 1 supercells). For example, the configurational entropies at high temperature limit for all supercells have clear deviation from that of the ideal fully disordered system, approximately 11.0%, 6.0%, and 3.8% for $Ca_{0.5}Zn_{0.5}CO_3$ of 2 × 2 × 1, 3 × 3 × 1, and 4 × 4 × 1 supercells, respectively (Fig. 3a). Although the convergence is not sufficient, configurational entropy is still a good measure for evaluating the degree of ion ordering in equilibrated systems.

Fig. 3b shows the variation of mixing entropy isotherms based on the calculation of a 2 × 2 × 1 supercell with Eq. 6, where the dash line represent the high temperature limit of this supercell size. Fig. 3b indicates significant ordering as temperature is

242 below 1500 K for various compositions. Even at high temperatures (>2500 K), ion
243 ordering in $Ca_{0.5}Zn_{0.5}CO_3$ is also evident. Except the composition of 1/24 or 23/24
244 substitution in a 2 × 2 × 1 supercell due to only one inequivalent substitution site,
245 there are many inequivalent configurations for all other compositions, and then
246 configurational entropy increases with temperature to fully disordered states.

247 The most stable configuration (i.e. with the lowest energy in configurational spectra)
248 for each composition is closely consistent with the ordering of ion substitution. From
249 the most stable configurations for x=1/6, 1/3, and 1/2 of 2 × 2 × 1 supercell shown in
250 Fig. 4, it is clear that the incorporated Zn^{2+} tends to occur at the sites neighboring to
251 another mixed Zn^{2+} within a (0001) layer, but the substituted layer will be segregated
252 by pure calcite layers. Particularly, the most stable configuration of $Ca_{0.5}Zn_{0.5}CO_3$ is
253 the same to the structure of minrecordite (Fig. 4c), where layers of smithsonite and
254 calcite alternate along the c axis. Such structures also coincide with $(Mn,Ca)CO_3$ solid
255 solutions previously disclosed by experimental study (Katsikopoulos et al. 2009) and
256 simulations (Wang et al. 2011).

257 A cluster expansion method based on calculation of excess energy of a binary
258 $(A_xB_{1-x})R$ solid solution by Eq. 9 has been used to illustrate substituting behavior.

259 $$\Delta E = \sum_n f_{AB(n)} J_n \qquad \text{Eq.9}$$

260 where $f_{AB(n)}$ is half the number of pairs clusters of AB type at the nth distance within
261 the supercell, and J_n is the effective pair interaction at the nth distance. J_n can be
262 predicted via a mechanical mixture of J_{Ca} and J_{Zn} which can be easily derived with

DDM (Vinograd et al. 2009).

$$J_n = xJ_{\mathrm{Zn}} + (1-x)J_{\mathrm{Ca}} \qquad \text{Eq.10}$$

The importance of *Js* decreases with the pair distance, and two important *Js* correspond to the distance 4.048 Å and 4.99 Å (Fig. 5), which represent the distance of the nearest cation pairs from two neighbor layers and within a layer, respectively. *J*s of these nearest pairs within a layer is positive, whereas those for interlayer pairs are negative. Because the structure shown in Figure 4c permits the most cation pairs of distance 4.048 Å and the least cation pairs of 4.99 Å, its Δ*E*, the sum of Eq. 9, is the lowest, and thus it is the most stable configuration. So, a simple interaction model for all compositions can be proposed, i.e. Zn-Zn (or Ca-Ca) interactions are favorable within a (0001) layer but unfavorable between layers, and Zn-Ca is the opposite.

Mixing enthalpy and free energy

The enthalpy and free energy of mixing can be calculated from the follow equations:

$$\Delta H_{mix} = H[\mathrm{Zn}_x\mathrm{Ca}_{1-x}\mathrm{CO}_3] - xH[\mathrm{ZnCO}_3] - (1-x)H[\mathrm{CaCO}_3] \qquad \text{Eq.11}$$

$$\Delta G_{mix} = G[\mathrm{Zn}_x\mathrm{Ca}_{1-x}\mathrm{CO}_3] - xG[\mathrm{ZnCO}_3] - (1-x)G[\mathrm{CaCO}_3] \qquad \text{Eq.12}$$

where $H[\mathrm{Zn}_x\mathrm{Ca}_{1-x}\mathrm{CO}_3]$, $G[\mathrm{Zn}_x\mathrm{Ca}_{1-x}\mathrm{CO}_3]$ is the enthalpy and free energy of $\mathrm{Zn}_x\mathrm{Ca}_{1-x}\mathrm{CO}_3$ calculated with Eq.3 and Eq.4 based on configurational statistics method, and $H[\mathrm{ZnCO}_3]$, $G[\mathrm{ZnCO}_3]$ and $H[\mathrm{CaCO}_3]$, $G[\mathrm{CaCO}_3]$ are for pure calcite and smithsonite. Here, the average lattice energy is thought equal to the actual enthalpies because the vibrational contribution to mixing enthalpies (~1%) is too little to be

284 accounted (Benny et al. 2009; Ruiz-Hernandez et al. 2010; Wang et al. 2011).

285 For 2 × 2 × 1 supercell model, the enthalpy isotherms at a set of temperatures from
286 273.15 K to 3000 K, were calculated as well as the enthalpy isotherm at the high
287 temperature limit (Fig. 6), at which all configurations are only weighted by their
288 degeneracies regardless of the Boltzmann factor. At the high temperature limit, the
289 enthalpy for the whole range of composition are positive. But, at finite temperatures
290 (< 2000 K), the enthalpies of highly substituted solid solutions decrease to negative
291 values. Although the calcite-smithsonite solid solutions at higher temperature are not
292 real cases, theoretically the corresponding configurations perhaps occur in some
293 non-equilibrated systems (Wang et al. 2011). At temperatures of reality, there are 5
294 local enthalpy minima at $ZnCO_3$ mole fraction of 1/6, 1/3, 1/2, 2/3, and 5/6
295 respectively, which is attributed to the reduced lattice energy caused by partial
296 ordering of substituted cations in the supercell. It is clear that the enthalpies of
297 compositions with $x > 0.5$ are higher than those with $x < 0.5$, thus all the isotherms are
298 asymmetric.

299 The free energies are prominent negative at high temperatures (>1500 K) for the
300 whole composition range (Fig. 7). But at lower temperatures (<1200 K), the solid
301 solutions with $1/3<x<2/3$ still stand negative free energies while those around both
302 end members have positive values at some low temperatures (<1200 K). Similarly to
303 the enthalpy, there are also 5 local minima at x=1/6, 1/3, 1/2, 2/3, and 5/6 respectively
304 due to the separately distribution of only fully Zn-substituted layers in these solid

solutions. The asymmetry of free energy isotherms and enthalpy implies that a substitution of Zn^{2+} into calcite costs less energy than Ca^{2+} into smithsonite because substituting a smaller cation (Zn^{2+}) into a site occupied by large cation is generally easier than a reverse process (Goldsmith 1983). Also, a smaller cation (Zn^{2+}) substituting a large cation generally causes less elastic strain in the lattice (McLean 1957; de Leeuw and Parker 2000; de Leeuw 2002).

Cell parameters

From the configurational spectrum of a 2 × 2 × 1 supercell, the cell parameter *c* and volume *V* can be obtained directly by configurational average of the c_m and V_m by using Eq. 5. However, the rotational symmetry of the hexagonal cell may be broken because the direct average of a_m may be different from the direct average of b_m. So, here a modified equation (Eq. 13) was used to calculate cell parameters.

$$a = (\sum_{m=1}^{M} P_m \mid a_m \times b_m \mid)^{\frac{1}{2}} \qquad \text{Eq.13}$$

where $|a_m \times b_m|$ is a constant within a set of equivalent configurations. The cell parameters and volume vary with composition (Fig. 8). The *a*, *c,* and volume of unit cell decrease with Zn^{2+} substitution increasing because the ionic radius of Zn^{2+} is smaller than Ca^{2+}. But as shown in Fig. 8b and 8d, only *a* shows a linear correlation with composition, which is in accord with Vegard's Law (West 1984). Whereas, *c* and *V* have a significant deviation from the mechanical mixture, especially the composition of $Ca_{0.5}Zn_{0.5}CO_3$, suggesting that partial ordering of substituted cations in the supercell prominently affects those parameters.

Phase relationship

The phase relations of calcite-smithsonite solid solution can be derived from the free energy isotherms with common tangent analysis (Vinograd et al. 2007a, 2009). The solid solution with composition $Zn_xCa_{1-x}CO_3$ is unstable or metastable if there is a pair of compositions has lower mechanical mixture free energy $E_{\text{mix } a,b}$ (here $a<x<b$). Thus, the phase diagram for this system can be outlined and two miscibility gaps separated by minrecordite field were disclosed (Fig. 9). The phase diagram is exactly similar to other carbonate solid solutions (Vinograd et al. 2007a, 2009). It is clear that the phase diagram is asymmetric, at a certain temperature the incorporated Zn into calcite is higher than Ca into smithsonite, which is consistent again with that substitution of Zn^{2+} into calcite costs less energy than Ca^{2+} into smithsonite.

Because calcite is the most common carbonate mineral in nature and many trace metal elements generally accommodate into its lattice, incorporating capacity of heavy metals into calcite have attracted high attentions. There are lots of reports on Zn-bearing calcite in literatures while little data about Ca-bearing smithsonite. From the phase diagram, especially the data around two end members, we can get the result that the content of Zn in calcite is very low (about 1.6 wt% at 600 K), and vice versa (about 0.48 wt% at 600 K). It coincides with the experimental results 250-1200 ppm of synthetic Zn-containing calcites (Lamble et al. 1997; Reeder et al. 1999), but is weakly consistent with some other data of coprecipitation calcite by EPMA (Temmam et al. 2000), in which the content of Zn can be up to 14700 ppm. In addition, it seems

347 inconsistent with the content of Zn up to 7.71 wt% in calcite (Liu et al. 2009). But it
348 should be noticed that all the high Zn contents are positively correlated with high Mn
349 contents . That is to say, the incorporation of Mn may enhance the substitution of Zn
350 (Temmam et al. 2000). On the other hand, most of the experimental content of Ca in
351 natural smithsonite by EPMA based on natural Ca-bearing smithsonite (Boni et al.
352 2007, 2009; Balassone et al. 2008; Coppola et al. 2008) are under the theoretical
353 maximum content derived from Fig. 9. We checked the data which are not consistent
354 with the theoretical estimation and again found that they are more or less affected by
355 incorporation of other elements, e.g. Fe and Pb.

356 Ciobanu et al. (2011) and his colleagues suggested that there may form
357 nanoparticles (<100 nm) or nano-scale lamellae during replacement processes of the
358 formation of mineral solid solutions, and disordered intergrowths between two end
359 mineral members maybe occur. Both heterogeneous phenomena can only be
360 visualized by transmission electron microscope (TEM) and focussed ion
361 beam–scanning electron microscopy (FIB–SEM), and the normally invisible phases
362 which are rich in exotic elements, will lead to high contents of incorporated impurity,
363 which is measured as locally homogeneous by normal experimental analysis
364 techniques like EMPA or *in situ* LA-ICPMS (Cook et al. 2009). Besides, some
365 coexisting substitutions, for example, the incorporation of Zn and Mn into calcite, Au
366 and As into pyrite (Chen et al. 2013), Ag and Sb into galena (Renock and Becker
367 2011), occur in the growth process of natural minerals, which can lead to higher

content of both two elements.

IMPLICATIONS

As calcite can accommodate various metals by calcium ion substitution. Zinc is a common element found in calcite as well as calcium in smithsonite. But, the substituting capacity and thermodynamically favored structures have not been well disclosed up to date. This study presents a simulation study on the thermodynamics of mixing of calcite-smithsonite solid solutions

Based on static calculation of all independent configurations of calcite-smithsonite solid solution with different compositions, substitutions within a (0001) cation layer are thermodynamically favored. Such phenomenon may be universal in all carbonates. It also confirms that the structures similar to dolomite are stable phases of carbonate solid solutions, where layers of two different cations regularly alternate along the *c* axis. Furthermore, other solid solutions only with completely replaced layers may be metastable phases.

The derived phase diagram and thermodynamic properties in this study can highlight studies on various issues although the present data may be slightly scattered . Firstly, the thermodynamic calculation will help the investigation of element partitioning between aqueous solution and solid solution systems. Secondly, the diagram can be used to discern the equilibrium maximum content of impurity ions under given condition, or to give a constraint on crystallization temperatures and/or solution chemistry. New geological thermometers may be found based on the detailed investigation of mineral solid solutions. Meanwhile, if the content of impurity in a

391 mineral grain is much higher than the equilibrium maximum content discerned from
392 the phase diagram, effects from crystallization environment, other impurity elements
393 and/or exsolution in nano-scale or nanoparticle inclusions, which cannot be
394 distinguished by common instrumental techniques, should be considered first.
395 In addition, this study further confirms that computer simulation is an available
396 method for thermodynamic study on solid solutions when experimental study is
397 scarce.
398

ACKNOWLEDGMENTS

The authors thank the two anonymous reviewers for the helpful comments and suggestions. This research was supported by the National Basic Research Program of China (973 program, 2014CB846004) and National Science Foundation of China (41272056 and 40930742). We are grateful to the High Performance Computing Center of Nanjing University for using the IBM Blade cluster system.

405 **REFERENCES CITED**

406 Austen, K.F., Wright, K., Slater, B., and Gale, J.D. (2005) The interaction of dolomite surfaces with
407 metal impurities: a computer simulation study. Physical Chemistry Chemical Physics, 7,
408 4150-4156.

409 Balassone, G., Rossi, M., Boni, M., Stanley, G., and McDermott, P. (2008) Mineralogical and
410 geochemical characterization of nonsulfide Zn–Pb mineralization at Silvermines and Galmoy
411 (Irish Midlands). Ore Geology Reviews, 33, 168-186.

412 Becker, U., Fernandez-Gonzalez, A., Prieto, M. Harrison, R., and Putnis, A. (2000) Direct calculation
413 of thermodynamic properties of the barite/celestite solid solution from molecular principles.
414 Physics and Chemistry of Minerals, 27, 291-300.

415 Benny, S., Grau-Crespo, R., and de Leeuw, N.H., (2009) A theoretical investigation of α-Fe_2O_3-Cr_2O_3
416 solid solutions. Physical Chemistry Chemical Physics, 11, 808-815.

417 Bickle, M.J. (2009) Geological carbon storage. Nature Geoscience, 2, 815-818.

418 Boni, M., Gilg, H.A., Balassone, G., Schneider, J., Allen, C., and Moore, F. (2007) Hypogene Zn
419 carbonate ores in the Angouran deposit, NW Iran. Mineralium Deposita, 42, 799-820.

420 Boni, M., Balassone, G., Arseneau, V., and Schmidt, P. (2009) The Nonsulfide Zinc Deposit at Accha
421 (Southern Peru): Geological and Mineralogical Characterization. Economic Geology, 104,
422 267-289.

423 Born, M., Huang, K., and Britain, G. (1954) Dynamical theory of crystal lattices. Clarendon Press,
424 Oxford.

425 Chen, A., Zhao, Z.w., Jia, X., Long, S., Huo, G., and Chen, X. (2009) Alkaline leaching Zn and its

426 concomitant metals from refractory hemimorphite zinc oxide ore. Hydrometallurgy, 97(3–4),
427 228-232.
428 Chen, J.H., Li, Y.Q., and Zhong, S.P. (2013) DFT simulation of the occurrences and correlation of gold
429 and arsenic in pyrite. American Mineralogist, 98, 1765-1771.
430 Ciobanu, C.L., Cook, N.J., Utsunomiya, S., Pring, A., and Green, L. (2011) Focussed ion
431 beam–transmission electron microscopy applications in ore mineralogy: Bridging micro- and
432 nanoscale observations. Ore Geology Reviews, 42, 6-31.
433 Connolly, J., and Williams, A. (1983) Density-functional theory applied to phase transformations in
434 transition-metal alloys. Physical Review B, 27, 5169.
435 Cook, N.J., Ciobanu, C.L., Pring, A., Skinner, W., Shimizu, M., Danyushevsky, L., Saini-Eidukat, B.,
436 and Melcher, F. (2009) Trace and minor elements in sphalerite: A LA-ICPMS study.
437 Geochimica et Cosmochimica Acta, 73(16), 4761-4791.
438 Cook, N.J., Ciobanu, C.L., Danyushevsky, L.V., and Gilbert, S. (2011) Minor and
439 trace elements in bornite and associated Cu–(Fe)-sulfides: A LA-ICP-MS
440 study. Geochimica et Cosmochimica Acta, 75(21), 6473-6496.
441 Coppola, V., Boni, M., Gilg, H.A., Balassone, G., and Dejonghe, L. (2008) The “calamine” nonsulfide
442 Zn–Pb deposits of Belgium: Petrographical, mineralogical and geochemical characterization.
443 Ore Geology Reviews, 33, 187-210.
444 Crocket, J.H., and Winchester, J.W. (1966) Coprecipitation of zinc with calcium carbonate.
445 Geochimica et Cosmochimica Acta, 30, 1093-1109.
446 Curti, E. (1999) Coprecipitation of radionuclides with calcite: estimation of partition coefficients based

447 on a review of laboratory investigations and geochemical data. Applied Geochemistry, 14,
448 433-445.
449 Curti, E., Kulik, D., and Tits, J. (2005) Solid solutions of trace Eu (III) in calcite: Thermodynamic
450 evaluation of experimental data over a wide range of pH and pCO_2. Geochimica et
451 cosmochimica acta, 69, 1721-1737.
452 Dandekar, D.P., and Ruoff, A.L. (1968) Temperature Dependence of the Elastic Constants of Calcite
453 between 160 and 300 K. Journal of Applied Physics, 39, 6004-6009.
454 de Leeuw, N.H. (2002) Molecular Dynamics Simulations of the Growth Inhibiting Effect of Fe^{2+},
455 Mg^{2+}, Cd^{2+}, and Sr^{2+} on Calcite Crystal Growth. The Journal of Physical Chemistry B, 106,
456 5241-5249.
457 de Leeuw, N.H., and Parker, S.C. (2000) Modeling absorption and segregation of magnesium and
458 cadmium ions to calcite surfaces: Introducing $MgCO_3$ and $CdCO_3$ potential models. The
459 Journal of Chemical Physics, 112, 4326-4333.
460 Dick, B.G. Jr., and Overhauser, A.W. (1958) Theory of the dielectric constants of alkali halide crystals.
461 Physical Review, 112, 90-103.
462 Espiari, S., Rashchi, F., and Sadrnezhaad, S.K. (2006) Hydrometallurgical treatment of tailings with
463 high zinc content. Hydrometallurgy, 82(1–2), 54-62.
464 Feng, L., Yang, X., Shen, Q., Xu, M., and Jin, B. (2007) Pelletizing and alkaline leaching of powdery
465 low grade zinc oxide ores. Hydrometallurgy, 89(3–4), 305-310.
466 Ferriss, E.D.A., Ewing, R.C., and Becker, U. (2010) Simulation of thermodynamic mixing properties
467 of actinide-containing zircon solid solutions. American Mineralogist, 95, 229-241.

468 Gale, J.D. (1997) GULP: A computer program for the symmetry-adapted simulation of solids. Journal
469 of the Chemical Society, Faraday Transactions, 93, 629-637.
470 Gale, J.D. (2005) GULP: Capabilities and prospects. Zeitschrift für Kristallographie - Crystalline
471 Materials, 220, 552-554.
472 Gale, J.D. and Rohl, A.L. (2003) The general utility lattice program (GULP). Molecular Simulation,
473 29, 291-341.
474 Glynn, P.D., and Reardon, E.J. (1990) Solid-solution aqueous-solution equilibria: thermodynamic
475 theory and representation. American Journal of Science, 290, 164-201.
476 Goldsmith, J.R. (1983) Phase relations of rhombohedral carbonates. Reviews in Mineralogy and
477 Geochemistry, 11, 49-76.
478 Graf, D.L. (1961) Crystallographic tables for the rhombohedral carbonates. American Mineralogist, 46,
479 1283-1316.
480 Grau-Crespo, R., de Leeuw, N.H., and Catlow, C.R.A. (2004) Distribution of Cations in $FeSbO_4$: A
481 Computer Modeling Study. Chemistry of Materials, 16, 1954-1960.
482 Grau-Crespo, R., Hamad, S., Catlow, C.R.A., and Leeuw, N.H.d. (2007) Symmetry-adapted
483 configurational modelling of fractional site occupancy in solids. Journal of Physics:
484 Condensed Matter, 19, 256201.
485 Grau-Crespo, R., de Leeuw, N.H., Hamad, S., and Waghmare, U.V. (2011) Phase separation and
486 surface segregation in ceria–zirconia solid solutions. Proceedings of the Royal Society A:
487 Mathematical, Physical and Engineering Science, 467, 1925-1938.
488 Haider, S., Grau-Crespo, R., Devey, A.J., and de Leeuw, N.H. (2012) Cation distribution and mixing

thermodynamics in Fe/Ni thiospinels. Geochimica Et Cosmochimica Acta, 88, 275-282.

Herzog, H.J. (2001) Peer Reviewed: What Future for Carbon Capture and Sequestration? Environmental Science & Technology, 35, 148A-153A.

Hume-Rothery, W., Smallman, R.E., and Haworth, C.W. (1969) The structure of metals and alloys. The Institute of Metals, London.

Irannajad, M., Ejtemaei, M., and Gharabaghi, M. (2009) The effect of reagents on selective flotation of smithsonite–calcite–quartz. Minerals Engineering, 22(9–10), 766-771.

Isaure, M.P., Sarret, G., Harada, E., Choi, Y.E., Marcus, M.A., Fakra, S.C., Geoffroy, N., Pairis, S., Susini, J., Clemens, S., and Manceau, A. (2010) Calcium promotes cadmium elimination as vaterite grains by tobacco trichomes. Geochimica et Cosmochimica Acta, 74, 5817-5834.

Jung, D.Y., Vinograd, V.L., Fabrichnaya, O.B., Oganov, A.R., Schmidt, M.W., and Winkler, B. (2010) Thermodynamics of mixing in $MgSiO_3$–Al_2O_3 perovskite and ilmenite from ab initio calculations. Earth and Planetary Science Letters, 295, 477-486.

Katsikopoulos, D., Fernández-González, Á., and Prieto, M. (2009) Precipitation and mixing properties of the "disordered" $(Mn,Ca)CO_3$ solid solution. Geochimica et Cosmochimica Acta, 73, 6147-6161.

Kulik, D.A., Vinograd, V.L., Paulsen, N., and Winkler, B., (2010) $(Ca,Sr)CO_3$ aqueous–solid solution systems: From atomistic simulations to thermodynamic modelling. Physics and Chemistry of the Earth, Parts A/B/C, 35, 217-232.

Lamble, G. Reeder, R. and Northrup, P. (1997) Characterization of heavy metal incorporation in calcite by XAFS spectroscopy. Le Journal de Physique IV, 7, C2-793-C2-797.

510 Liu, T., Wang, R.C., Lu, X.C., Li, J., and Hu, H., (2009) Highly Zn, Mn-rich calcite in calcareous tufa
511 from the Qixiashan Pb-Zn Mine, Nanjing: a possible candidate for Zn-Mn removal from
512 mining impacted waters. Chinese Science Bulletin, 54, 1376-1383.
513 Matter, J.M., and Kelemen, P.B. (2009) Permanent storage of carbon dioxide in geological reservoirs
514 by mineral carbonation. Nature Geoscience, 2, 837-841.
515 McLean, D. (1957) Grain boundaries in metals. Clarendon Press, Oxford.
516 Mehdilo, A., Irannajad, M., and Zarei, H. (2013) Smithsonite Flotation from Zinc Oxide Ore using
517 Alkyl Amine Acetate Collectors. Separation Science and Technology, 49(3), 445-457.
518 Mondillo, N., Boni, M., Balassone, G., and Grist, B. (2011) In search of the lost zinc: A lesson from
519 the Jabali (Yemen) nonsulfide zinc deposit. Journal of Geochemical Exploration, 108,
520 209-219.
521 Navidi Kashani, A.H., and Rashchi, F. (2008) Separation of oxidized zinc minerals from tailings:
522 Influence of flotation reagents. Minerals Engineering, 21(12–14), 967-972.
523 Reeder, R.J. (1983) Crystal chemistry of the rhombohedral carbonates. Reviews in Mineralogy and
524 Geochemistry, 11,1-47.
525 Reeder, R.J., Lamble, G.M., and Northrup, P.A. (1999) XAFS study of the coordination and local
526 relaxation around Co^{2+}, Zn^{2+}, Pb^{2+}, and Ba^{2+}, trace elements in calcite. American Mineralogist,
527 84, 1049-1060.
528 Reich, M., and Becker, U. (2006) First-principles calculations of the thermodynamic mixing properties
529 of arsenic incorporation into pyrite and marcasite. Chemical Geology, 225, 278-290.
530 Renock, D., and Becker, U. (2011) A first principles study of coupled substitution in galena. Ore

Geology Reviews, 42, 71-83.

Rohl, A.L., Wright, K., and Gale, J.D. (2003) Evidence from surface phonons for the (2 × 1) reconstruction of the (101□4) surface of calcite from computer simulation. American Mineralogist, 88, 921-925.

Ruiz-Hernandez, S.E., Grau-Crespo, R., Ruiz-Salvador, A.R., and De Leeuw, N.H. (2010) Thermochemistry of strontium incorporation in aragonite from atomistic simulations. Geochimica Et Cosmochimica Acta, 74, 1320-1328.

Sanchez, J.M., Ducastelle, F., and Gratias, D. (1984) Generalized cluster description of multicomponent systems. Physica A: Statistical Mechanics and its Applications, 128, 334-350.

Sarret, G., Isaure, M.P., Marcus, M.A., Harada, E., Choi, Y.E., Pairis, S., Fakra, S., and Manceau, A. (2007) Chemical forms of calcium in Ca, Zn- and Ca, Cd-containing grains excreted by tobacco trichomes. Canadian Journal of Chemistry, 85, 738-746.

Shannon, R. (1976) Revised effective ionic radii and systematic studies of interatomic distances in halides and chalcogenides. Acta Crystallographica Section A: Crystal Physics, Diffraction, Theoretical and General Crystallography, 32, 751-767.

Shi, Q., Feng, Q., Zhang, G., and Deng, H. (2012) Electrokinetic properties of smithsonite and its floatability with anionic collector. Colloids and Surfaces A: Physicochemical and Engineering Aspects, 410(0), 178-183.

Shi, Q., Zhang, G., Feng, Q., and Deng, H. (2013) Effect of solution chemistry on the flotation system of smithsonite and calcite. International Journal of Mineral Processing, 119(0), 34-39.

552 Temmam, M., Paquette, J., and Vali, H. (2000) Mn and Zn incorporation into calcite as a function of
553 chloride aqueous concentration. Geochimica et Cosmochimica Acta, 64, 2417-2430.
554 Todorov, I.T., Allan, N.L., Lavrentiev, M.Y., Freeman, C.L., Mohn, C.E., and Purton, J.A., (2004)
555 Simulation of mineral solid solutions at zero and high pressure using lattice statics, lattice
556 dynamics and Monte Carlo methods. Journal of Physics: Condensed Matter, 16, S2751-S2770.
557 Vinograd, V.L. and Sluiter, M.H.F. (2006) Thermodynamics of mixing in pyrope-grossular,
558 $Mg_3Al_2Si_3O_{12}$-$Ca_3Al_2Si_3O_{12}$, solid solution from lattice dynamics calculations and Monte
559 Carlo simulations. American Mineralogist, 91, 1815-1830.
560 Vinograd, V.L. and Winkler, B. (2010) An Efficient Cluster Expansion Method for Binary Solid
561 Solutions: Application to the Halite-Silvite, NaCl-KCl, System. Reviews in Mineralogy and
562 Geochemistry, 71, 413-436.
563 Vinograd, V.L., Winkler, B., Putnis, A., Gale, J.D., and Sluiter, M.H.F. (2006a) Static lattice energy
564 calculations of mixing and ordering enthalpy in binary carbonate solid solutions. Chemical
565 Geology, 225(3-4), 304-313.
566 Vinograd, V.L., Winkler, B., Putnis, A., Kroll, H., Milman, V., Gale, J.D., and Fabrichnaya, O.B.
567 (2006b) Thermodynamics of pyrope–majorite, $Mg_3Al_2Si_3O_{12}$–$Mg_4Si_4O_{12}$, solid solution from
568 atomistic model calculations. Molecular Simulation, 32, 85-99.
569 Vinograd, V.L., Burton, B.P., Gale, J.D., Allan, N.L., and Winkler, B. (2007a) Activity–composition
570 relations in the system $CaCO_3$–$MgCO_3$ predicted from static structure energy calculations and
571 Monte Carlo simulations. Geochimica Et Cosmochimica Acta, 71, 974-983.
572 Vinograd, V.L., Perchuk, L.L., Gerya, T.V., Putnis, A., Winkler, B., and Gale, J.D. (2007b)

Order/disorder phase transition in cordierite and its possible relationship to the development of symplectite reaction textures in granulites. Petrology, 15, 427-440.

Vinograd, V.L., Gale, J.D., and Winkler, B. (2007c) Thermodynamics of mixing in diopside–jadeite, $CaMgSi_2O_6$–$NaAlSi_2O_6$, solid solution from static lattice energy calculations. Physics and Chemistry of Minerals, 34, 713-725.

Vinograd, V.L., Bosbach, D., Winkler, B., and Gale, J.D. (2008) Subsolidus phase relations in $Ca_2Mo_2O_8$-$NaEuMo_2O_8$-powellite solid solution predicted from static lattice energy calculations and Monte Carlo simulations. Physical chemistry chemical physics, 10, 3509-18.

Vinograd, V.L., Sluiter, M.H.F., and Winkler, B. (2009) Subsolidus phase relations in the $CaCO_3$–$MgCO_3$ system predicted from the excess enthalpies of supercell structures with single and double defects. Physical Review B, 79, 104201.

Vinograd, V.L., Safonov, O.G., Wilson, D.J., Perchuk, L.L., Bindi, L., Gale, J.D., and Winkler, B. (2010a) Atomistic model of diopside-K-jadeite ($CaMgSi_2O_6$-$KAlSi_2O_6$) solid solution. Petrology, 18, 447-459.

Vinograd, V.L., Paulsen, N., Winkler, B., and van de Walle, A. (2010b) Thermodynamics of mixing in the ternary rhombohedral carbonate solid solution, $(Ca_xMg_y,Mn_{1-x-y})CO_3$, from atomistic simulations. CALPHAD: Computer Coupling of Phase Diagrams and Thermochemistry, 34, 113-119.

Wang, Q., and de Leeuw, N.H. (2008) A computer-modelling study of $CdCO_3$-$CaCO_3$ solid solutions. Mineralogical Magazine, 72, 525-529.

Wang, Q., Grau-Crespo, R., and de Leeuw, N.H. (2011) Mixing Thermodynamics of the

Calcite-Structured (Mn,Ca)CO_3 Solid Solution: A Computer Simulation Study. Journal of Physical Chemistry B, 115, 13854–13861.

West, A.R. (1984) Solid state chemistry and its applications. Wiley, New York.

Yeomans, J.M. (1992) Statistical mechanics of phase transitions. Oxford University Press, New York.

Zavarin, M., Roberts, S.K., Hakem, N., Sawvel, A.M., and Kersting, A.B. (2005) Eu (III), Sm (III), Np (V), Pu (V), and Pu (IV) sorption to calcite. Radiochimica Acta/International journal for chemical aspects of nuclear science and technology, 93, 93-102.

Zhang, J., and Reeder, R.J. (1999) Comparative compressibilities of calcite-structure carbonates: Deviations from empirical relations. American Mineralogist, 84, 861-870.

Zhao, Y.C., and Stanforth, R. (2000) Production of Zn powder by alkaline treatment of smithsonite Zn–Pb ores. Hydrometallurgy, 56,237-249.

606 **Figure captions**

607

608 **FIGURE 1.** The static lattice energy spectra and the distribution of all the

609 configurations with the composition of $Ca_{0.5}Zn_{0.5}CO_3$ in a 2 × 2 × 1 supercell.

610

611 **FIGURE 2.** Probabilities of the lowest 6 independent configurations of $Zn_{0.5}Ca_{0.5}CO_3$

612 and their summation with respect to temperature.

613

614 **FIGURE 3. (a)** Variation of the maximum entropy(high temperature limit) with

615 respect to different cell sizes. The dash line represents the configurational entropy of

616 an ideal fully disordered system. **(b)** Variation of the mixing entropy isotherms for the

617 2 × 2 × 1 supercell. The dash line represents the high temperature limit of this

618 supercell size.

619

620 **FIGURE 4.** The most stable configurations for x=1/6, 1/3 and 1/2 of 2 × 2 × 1

621 supercell. **4c** is the same to the structure of minrecordite.

622

623 **FIGURE 5.** The values of the effective pair interactions *Js* derived with DDM

624 (Vinograd et al. 2009)with respect to distance of the two interactive cations. Two lines

625 represent *Js* of the two end members, calcite and smithsonite, respectively.

626

627 **FIGURE 6.** The enthalpy isotherms at a set of temperatures from 273.15 K to 3000 K

628 and the high temperature limit as a function of mole fraction of $ZnCO_3$ for the 2 × 2 ×

629 1 supercell.

FIGURE 7. The free energy isotherms at a set of temperatures from 273.15 K to 3000 K as a function of mole fraction of $ZnCO_3$ for the 2 × 2 × 1 supercell.

FIGURE 8. Variation of the cell parameters and volume with composition, and the deviation of the cell parameters and volume from the mechanical mixture.

FIGURE 9. Phase diagram derived from the free energy isotherms with common tangent analysis.

639 **TABLE 1.** Potential parameters used in this study

Coulombic	Charge			
Ca，Zn	2.00			
C	1.34			
O core	1.02			
O shell	-2.13			
Buckingham	A(eV)	ρ(Å)	C(eV·Å^6)	Cutoff(Å)
O core-O core	4030.3	0.2455	0	Intra/2.5
O shell-O shell	64242.5	0.1989	21.8436	Inter/15.0
Ca-O shell	2154.06	0.2891	0	10.0
Zn-O shell	1029.39	0.2891	0	10.0
Spring	k (eV·Å^{-2})			
O	52.74			
Morse	D (eV)	α(Å^{-1})	r_0(Å)	
C-O core	5.00	2.5228	1.1982	Intra/Bonded
Three-body	k (eV·rad^{-2})	θ_0(°)		
O core-C-O core	1.7995	120.0		Intra/Bonded
Out of plane	k_2 (eV·Å^{-2})	k_2 (eV·Å^{-2})		
C-O core-O core-O core	8.6892	360.0		Intra/Bonded

640

641 **TABLE 2.** Experimental and calculated structural properties of calcite and
642 smithsonite

	Calcite			Smithsonite		
	Experiment	Calculated	Δ%	Experiment	Calculated	Δ%
a(Å)	4.99[a]	4.98	-0.2	4.65 [a]	4.64	-0.2
c(Å)	17.06 [a]	17.07	0.1	15.03 [a]	14.88	-1.0
c/a	3.42	3.43	0.3	3.23	3.21	-0.6
V($Å^3$)	367.9	366.8	-0.3	281.4	278.0	-1.2
B(GPa)	73[b]	77.1	5.6	123[c]	121.8	-1.0

643 a Cell parameters from Graf (1961)

644 b Calculated from experimental elastic constants of Dandekar and Ruoff (1968)

645 c Bulk moduli from Zhang and Reeder (1999)

TABLE 3. Tot number of configurations and independent configurations for each composition of $Zn_xCa_{1-x}CO_3$ in 2 × 2 × 1, 3 × 3 × 1 and 4 × 4 × 1 supercells

Cell composition	x or 1-x	Total number of configurations	Independent configurations
$A_{24}(CO_3)_{24}$	0.000	1	1
$A_{23}B_1(CO_3)_{24}$	0.042	24	1
$A_{22}B_2(CO_3)_{24}$	0.083	276	7
$A_{21}B_3(CO_3)_{24}$	0.125	2024	20
$A_{20}B_4(CO_3)_{24}$	0.167	10626	102
$A_{19}B_5(CO_3)_{24}$	0.208	42504	317
$A_{18}B_6(CO_3)_{24}$	0.250	134596	1033
$A_{17}B_7(CO_3)_{24}$	0.292	346104	2467
$A_{16}B_8(CO_3)_{24}$	0.333	735471	5330
$A_{15}B_9(CO_3)_{24}$	0.375	1307504	9219
$A_{14}B_{10}(CO_3)_{24}$	0.417	1961256	13980
$A_{13}B_{11}(CO_3)_{24}$	0.458	2496144	17520
$A_{12}B_{12}(CO_3)_{24}$	0.500	2704156	19219
$A_{53}B_1(CO_3)_{54}$	0.019	54	1
$A_{52}B_2(CO_3)_{54}$	0.037	1431	11
$A_{51}B_3(CO_3)_{54}$	0.056	24804	86
$A_{50}B_4(CO_3)_{54}$	0.074	316251	1051
$A_{49}B_5(CO_3)_{54}$	0.093	3162510	9829
$A_{95}B_1(CO_3)_{96}$	0.010	96	1
$A_{94}B_2(CO_3)_{96}$	0.021	4560	18
$A_{93}B_3(CO_3)_{96}$	0.031	142880	264
$A_{92}B_4(CO_3)_{96}$	0.042	3321960	5999

A and B stand for either Zn or Ca.

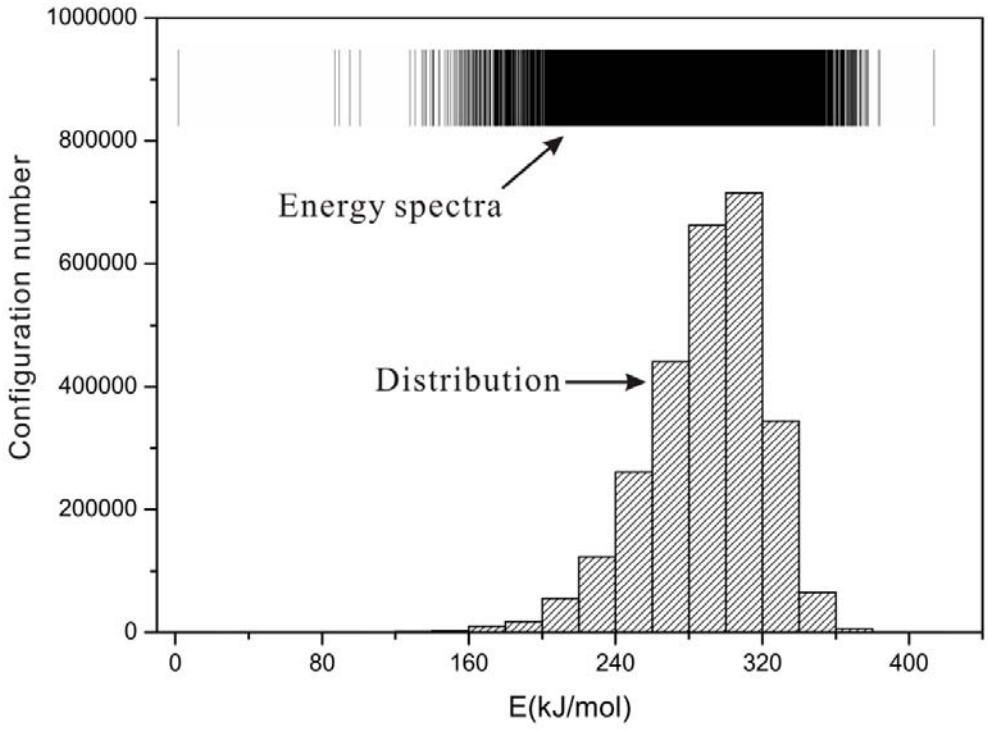
1000000
800000
600000
400000
200000
0
Configuration number
Energy spectra
Distribution
0
80
160
240
320
400
E(kJ/mol)

FIGURE 1.

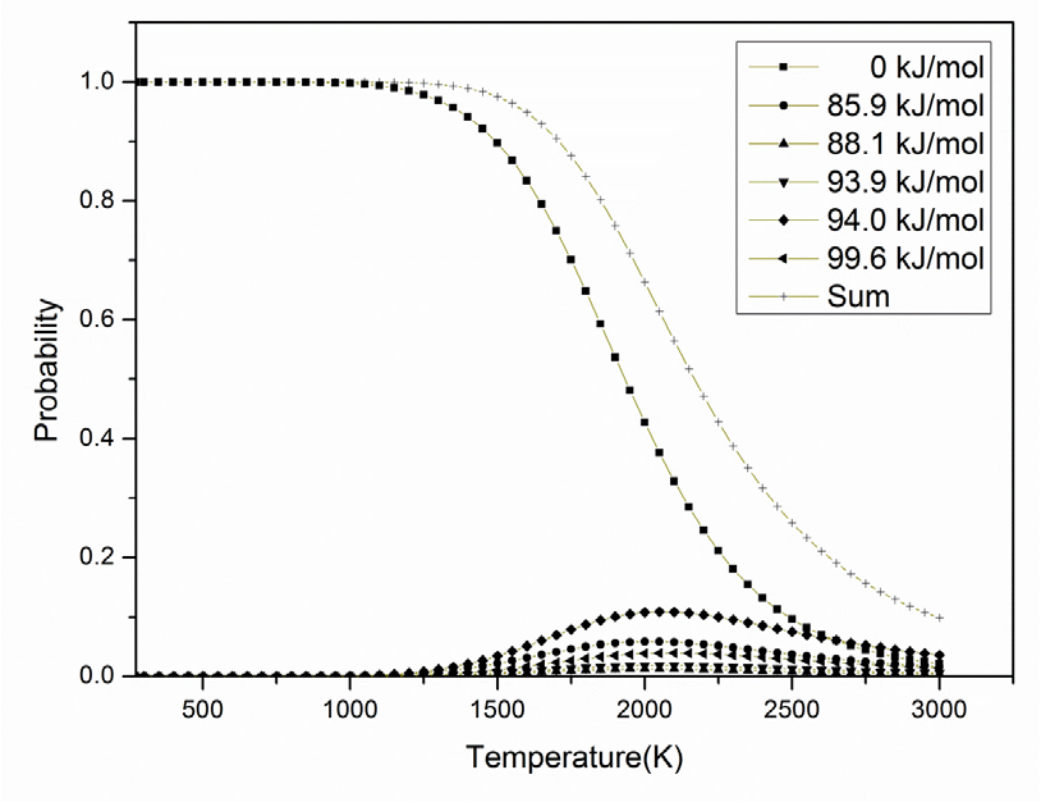
0 kJ/mol
85.9 kJ/mol
88.1 kJ/mol
93.9 kJ/mol
94.0 kJ/mol
99.6 kJ/mol
Sum
Probability
Temperature(K)
0.0
0.2
0.4
0.6
0.8
1.0
500
1000
1500
2000
2500
3000

FIGURE 2.

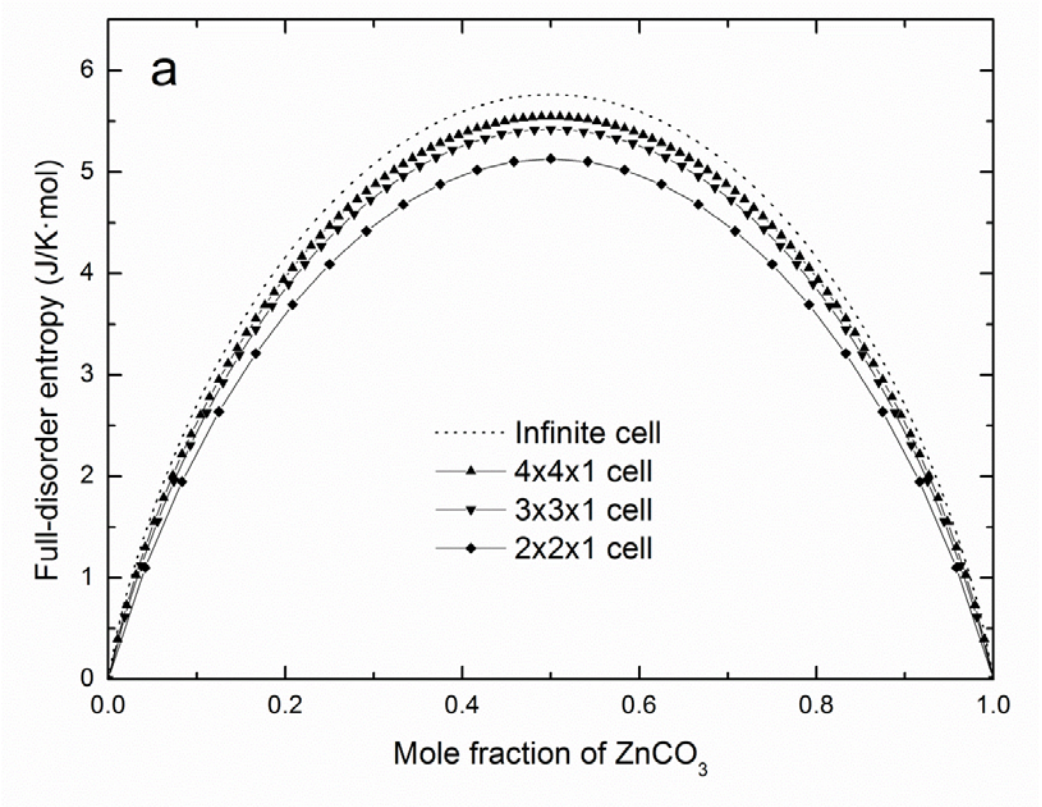
a
Full-disorder entropy (J/K·mol)
Mole fraction of ZnCO3
Infinite cell
4x4x1 cell
3x3x1 cell
2x2x1 cell
0
1
2
3
4
5
6
0.0
0.2
0.4
0.6
0.8
1.0

FIGURE 3a.

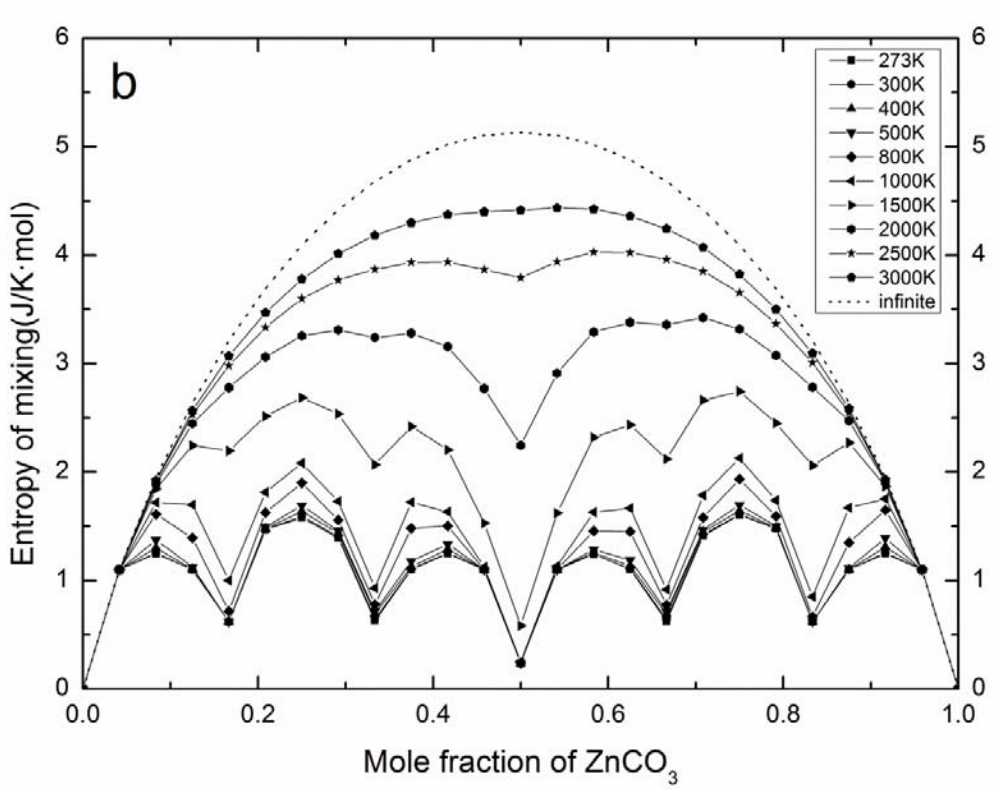
b
273K
300K
400K
500K
800K
1000K
1500K
2000K
2500K
3000K
infinite
Entropy of mixing(J/K·mol)
Mole fraction of ZnCO3
0
1
2
3
4
5
6
0.0
0.2
0.4
0.6
0.8
1.0

FIGURE 3b.

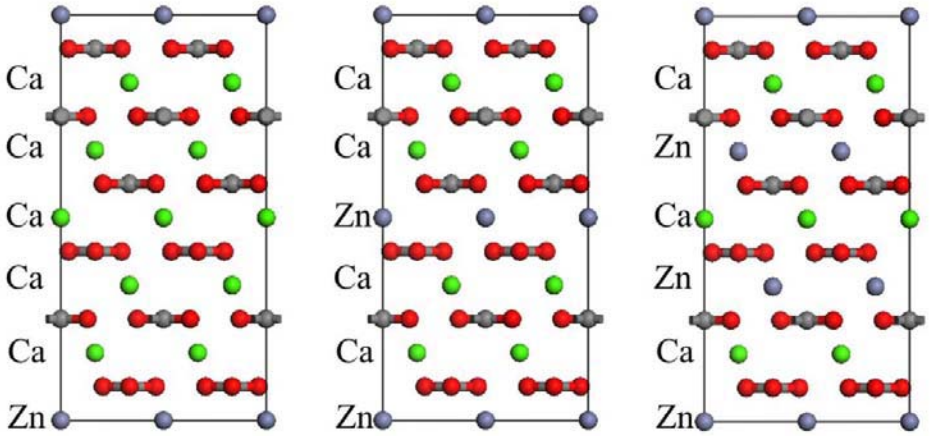

FIGURE 4.

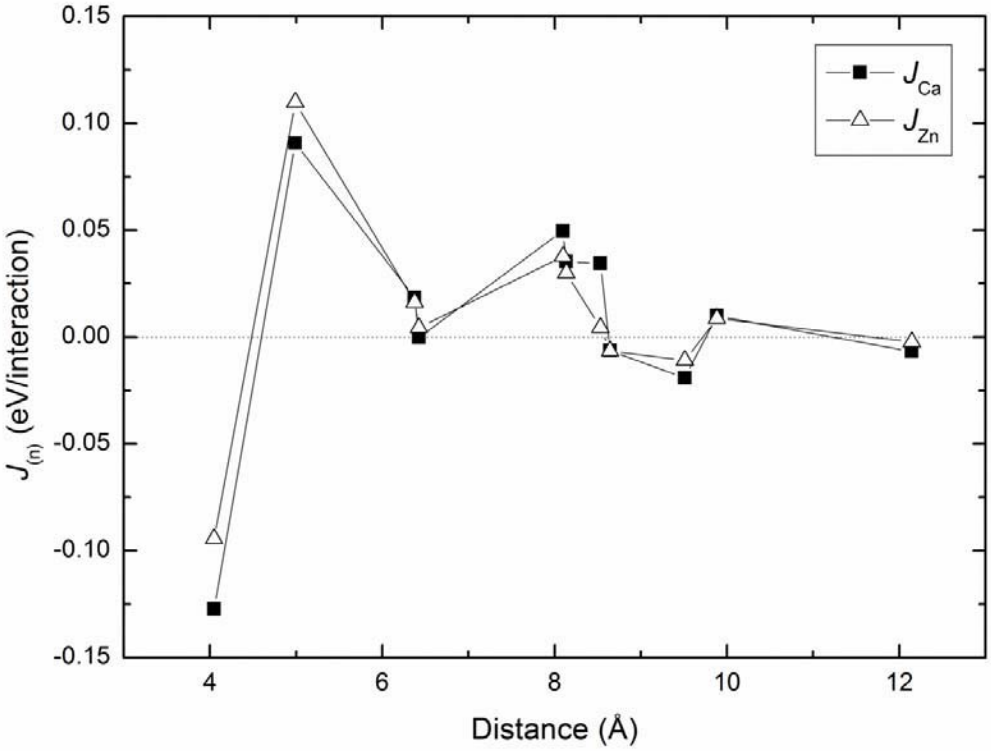
0.15
0.10
0.05
0.00
-0.05
-0.10
-0.15
$J_{(n)}$ (eV/interaction)
4
6
8
10
12
Distance (Å)
J_{Ca}
J_{Zn}

FIGURE 5.

25

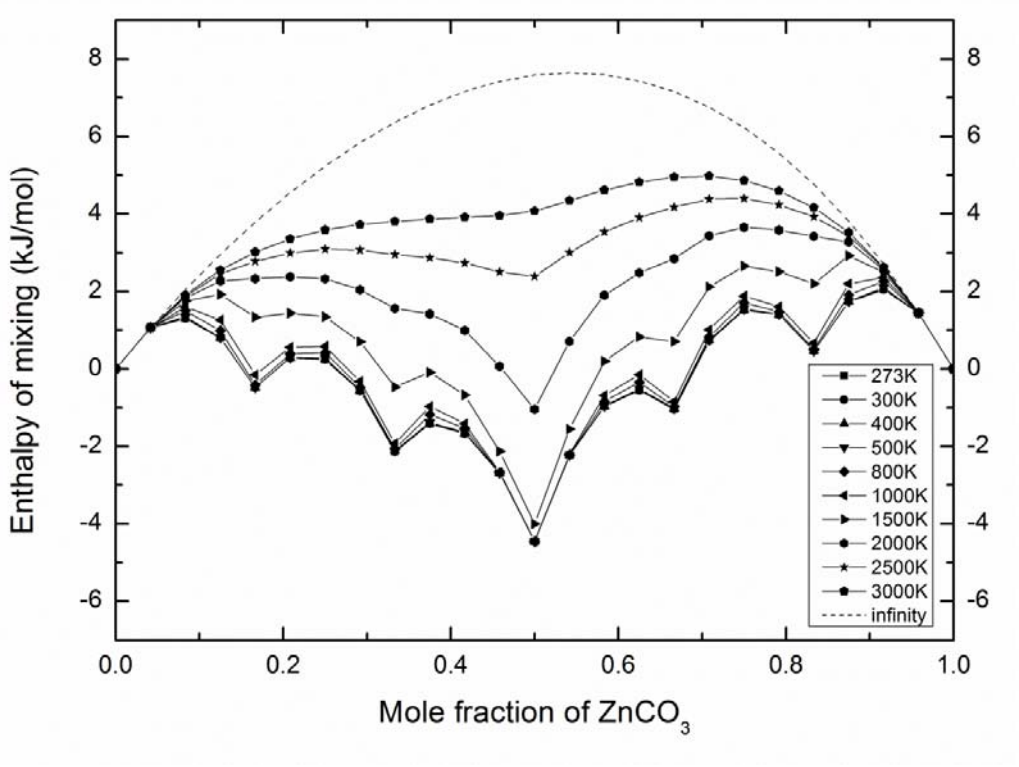

26

27 **FIGURE 6.**

28

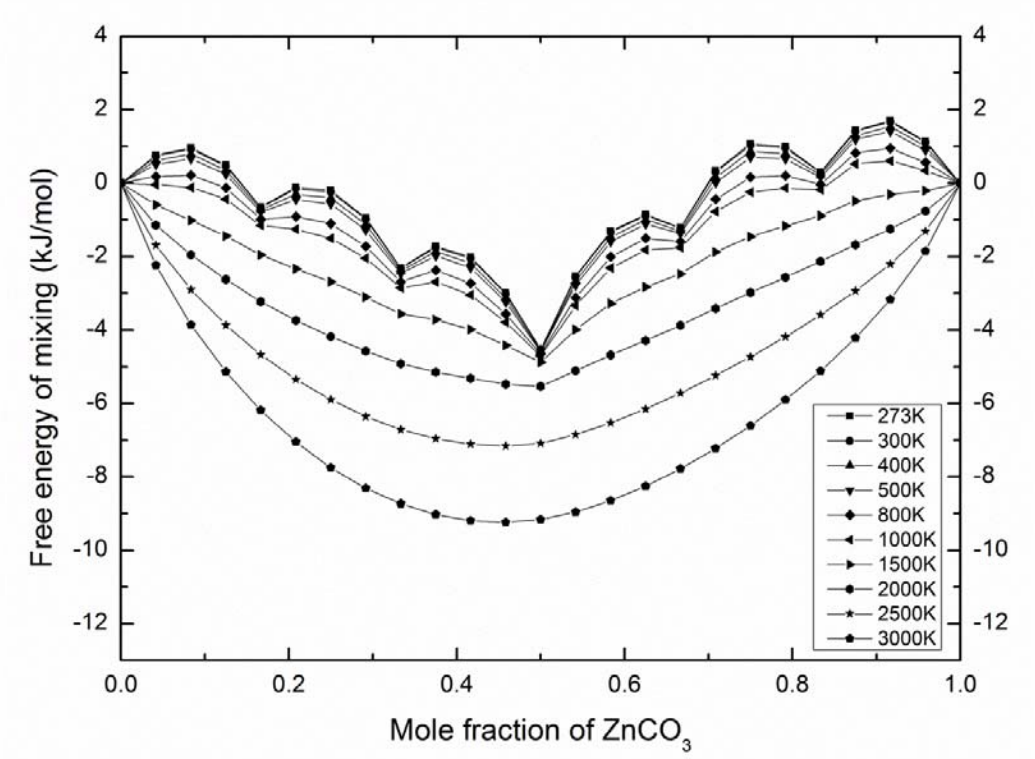
Free energy of mixing (kJ/mol)
Mole fraction of $ZnCO_3$
273K
300K
400K
500K
800K
1000K
1500K
2000K
2500K
3000K

FIGURE 7.

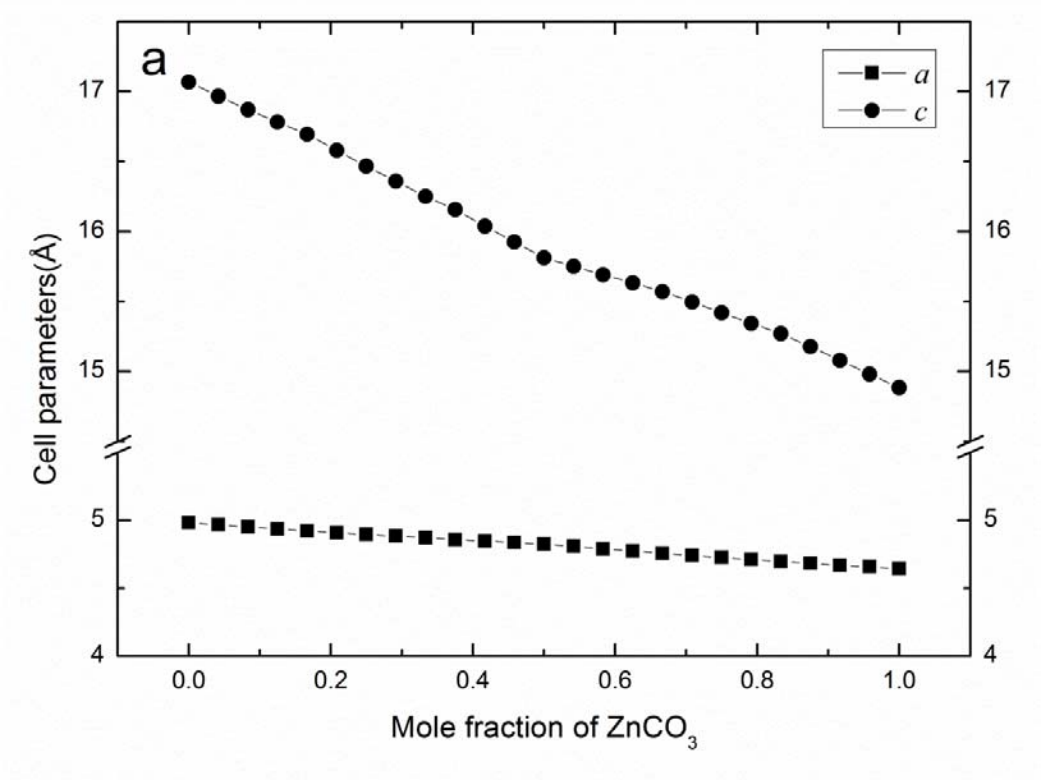
a
a
c
Cell parameters(Å)
17
16
15
5
4
0.0
0.2
0.4
0.6
0.8
1.0
Mole fraction of ZnCO3

FIGURE 8a.

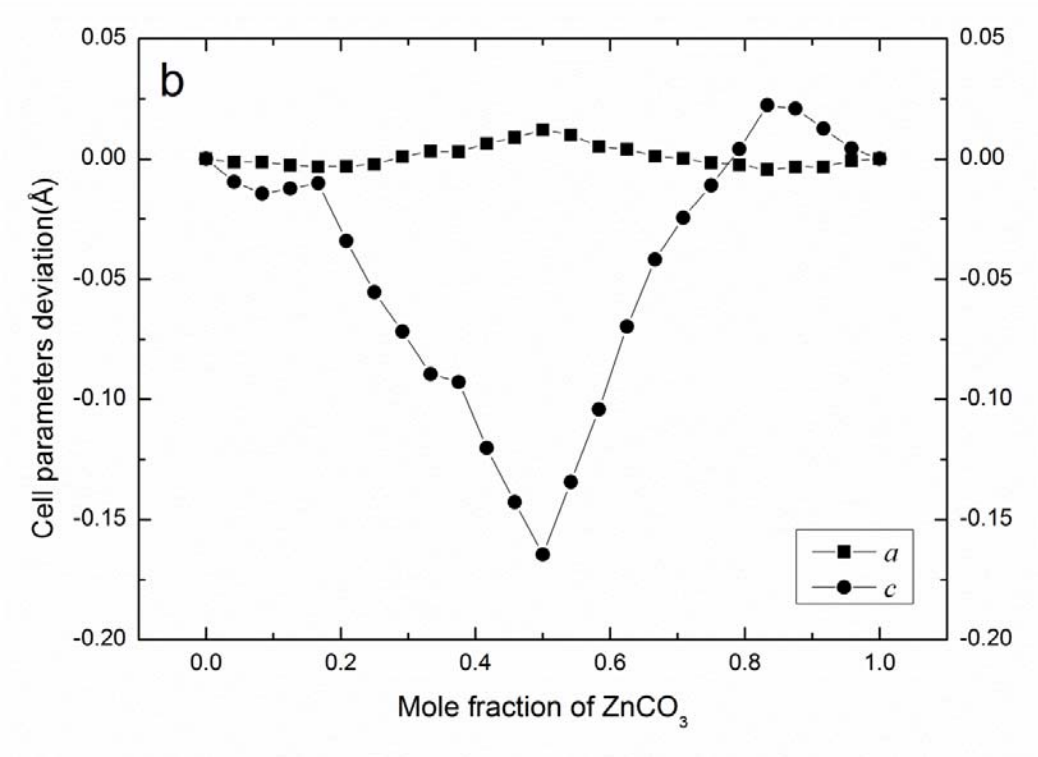
b
Cell parameters deviation(Å)
Mole fraction of ZnCO3
a
c
0.05
0.00
-0.05
-0.10
-0.15
-0.20
0.0
0.2
0.4
0.6
0.8
1.0

FIGURE 8b.

41

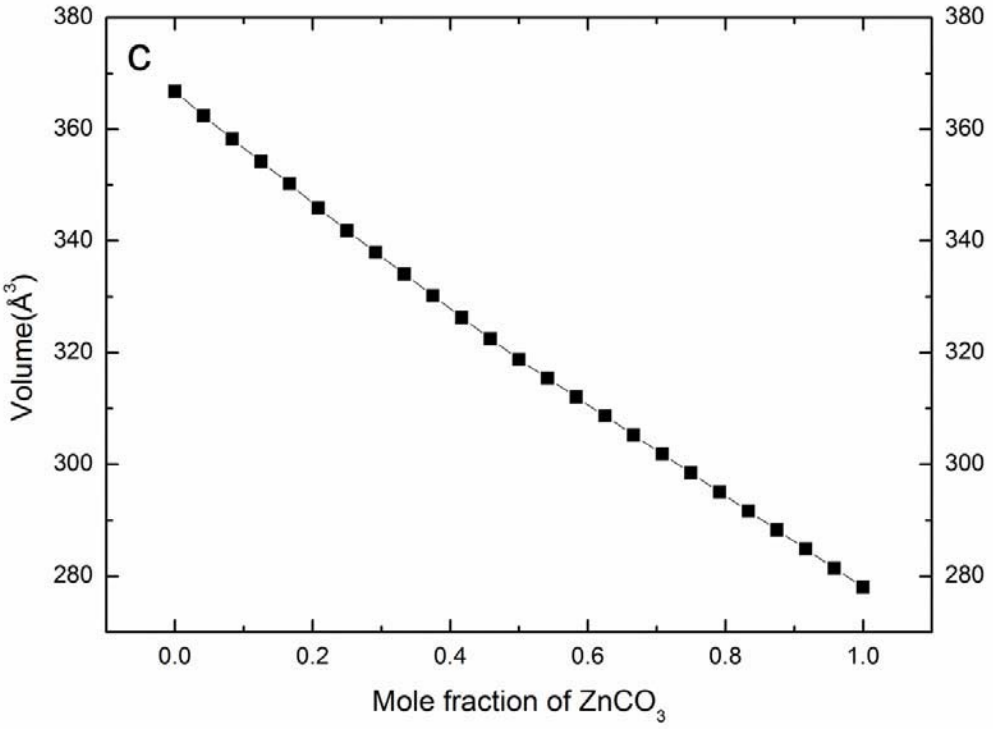

42

43 **FIGURE 8c.**

44

45

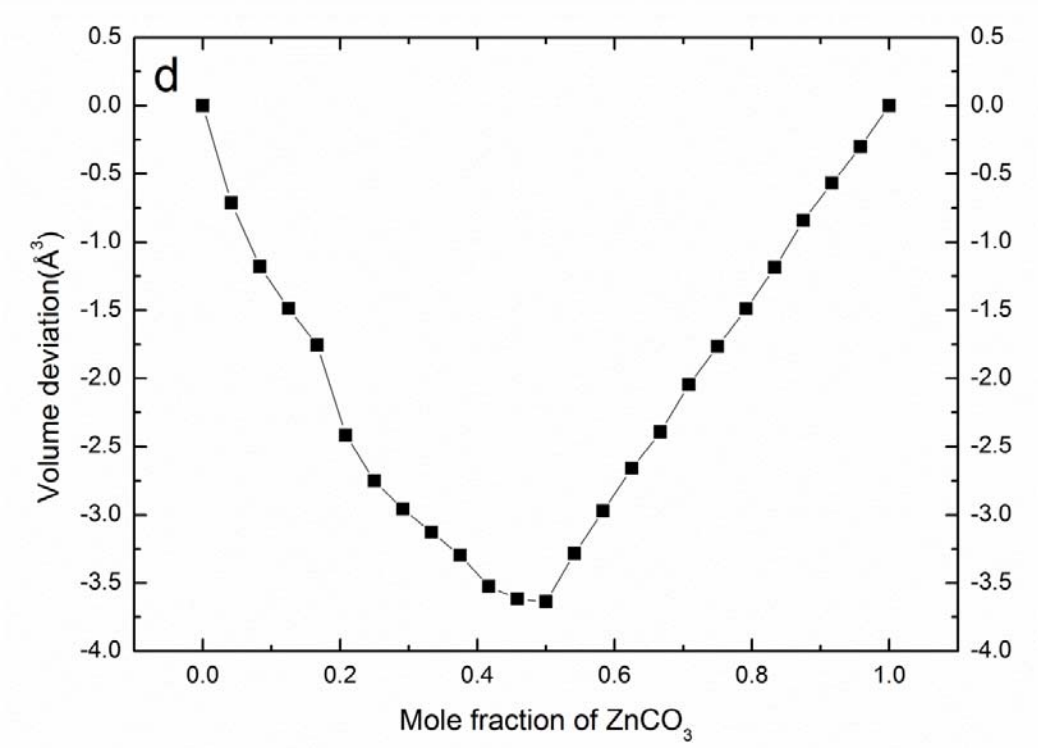

46

47 **FIGURE 8d.**

48

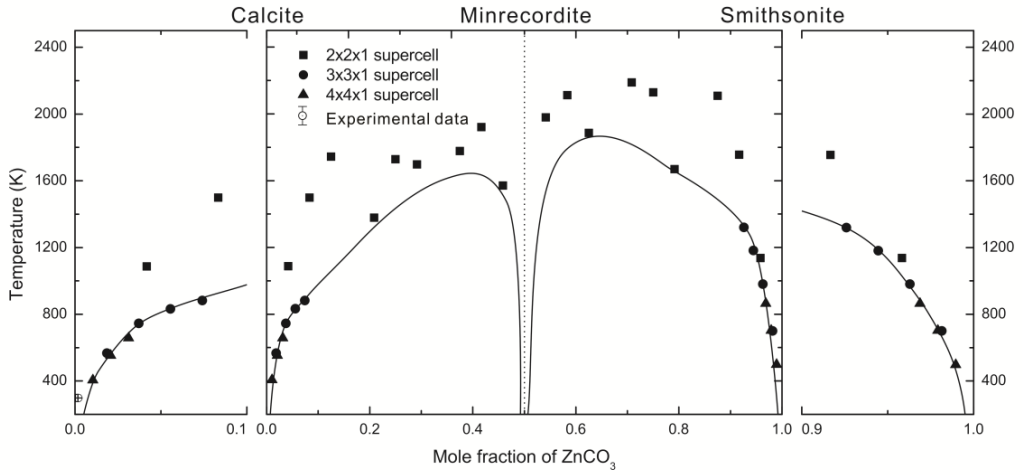
Calcite
Minrecordite
Smithsonite
2x2x1 supercell
3x3x1 supercell
4x4x1 supercell
Experimental data
Temperature (K)
Mole fraction of ZnCO3
2400
2000
1600
1200
800
400
0.0
0.1
0.2
0.4
0.6
0.8
1.0
0.9

FIGURE 9.

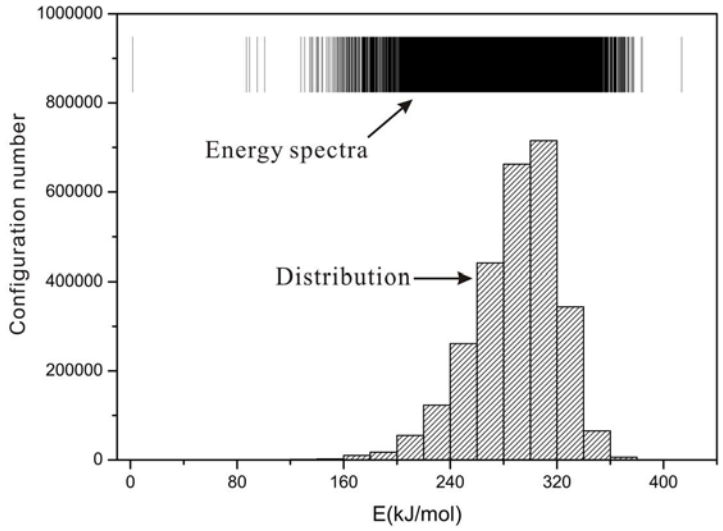
1000000
800000
600000
400000
200000
0
Configuration number
Energy spectra
Distribution
0
80
160
240
320
400
E(kJ/mol)

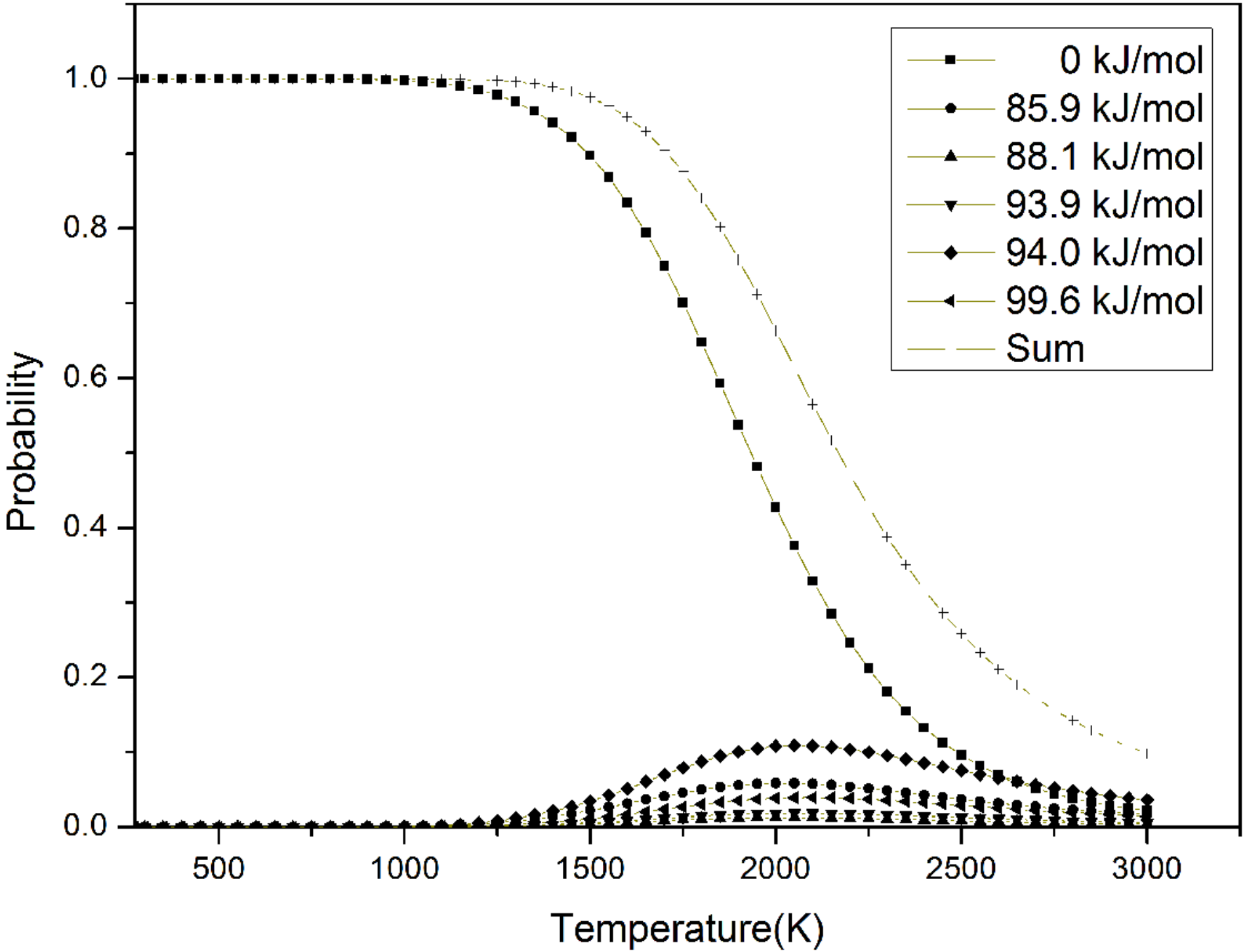
0 kJ/mol
85.9 kJ/mol
88.1 kJ/mol
93.9 kJ/mol
94.0 kJ/mol
99.6 kJ/mol
Sum
Probability
1.0
0.8
0.6
0.4
0.2
0.0
500
1000
1500
2000
2500
3000
Temperature(K)

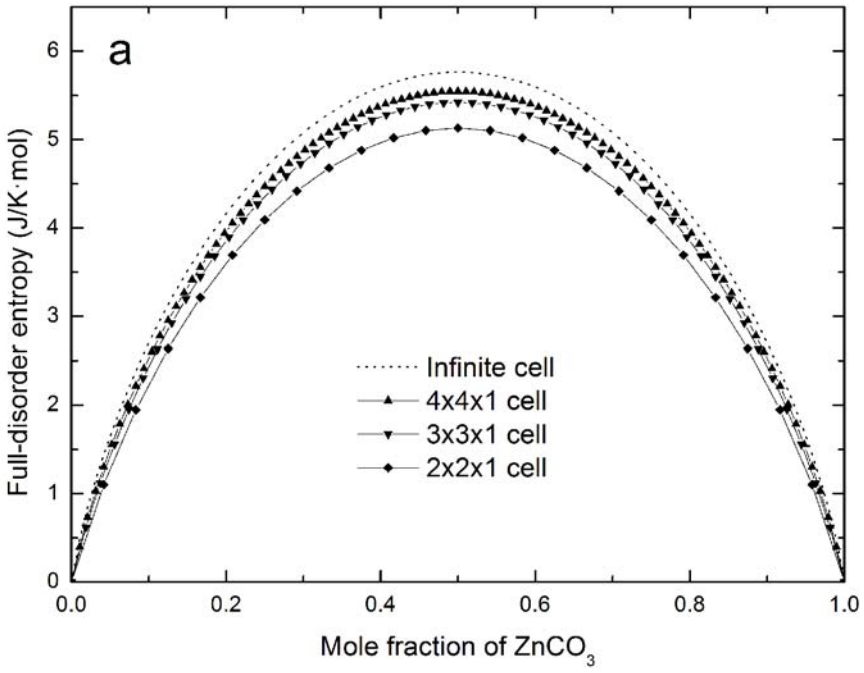
a
Full-disorder entropy (J/K·mol)
Mole fraction of ZnCO3
Infinite cell
4x4x1 cell
3x3x1 cell
2x2x1 cell
0
1
2
3
4
5
6
0.0
0.2
0.4
0.6
0.8
1.0

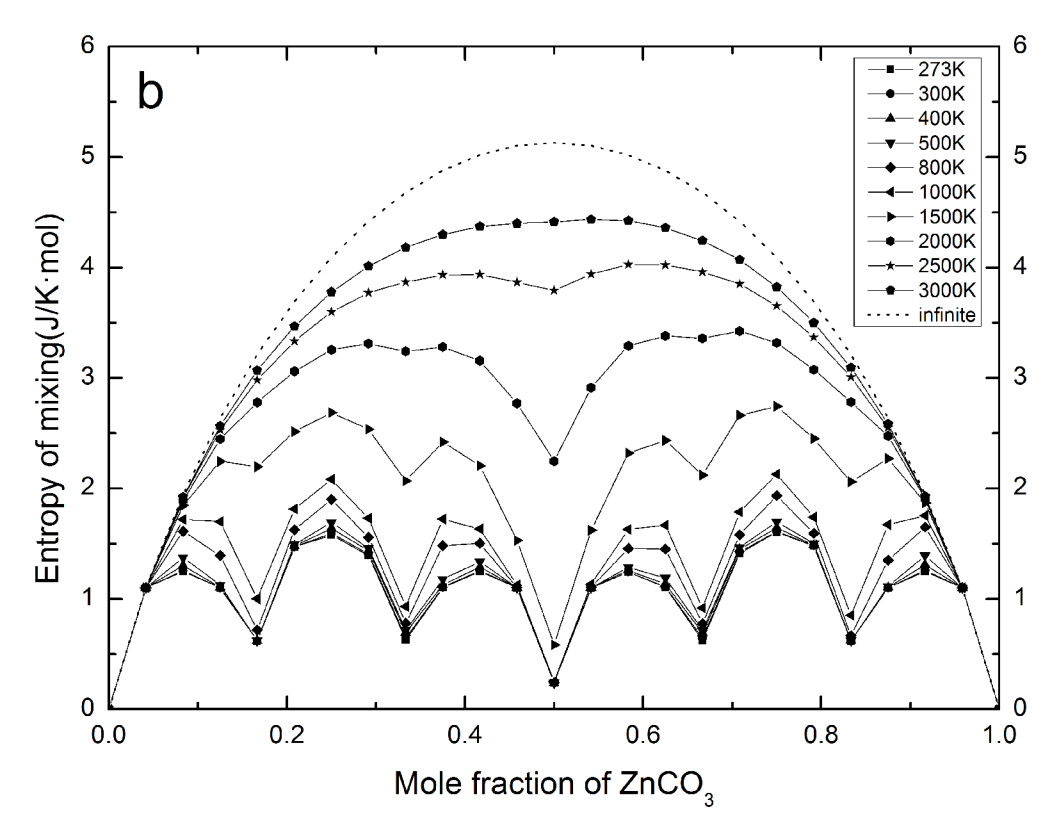
b
273K
300K
400K
500K
800K
1000K
1500K
2000K
2500K
3000K
infinite
Entropy of mixing(J/K·mol)
Mole fraction of ZnCO3
0
1
2
3
4
5
6
0.0
0.2
0.4
0.6
0.8
1.0

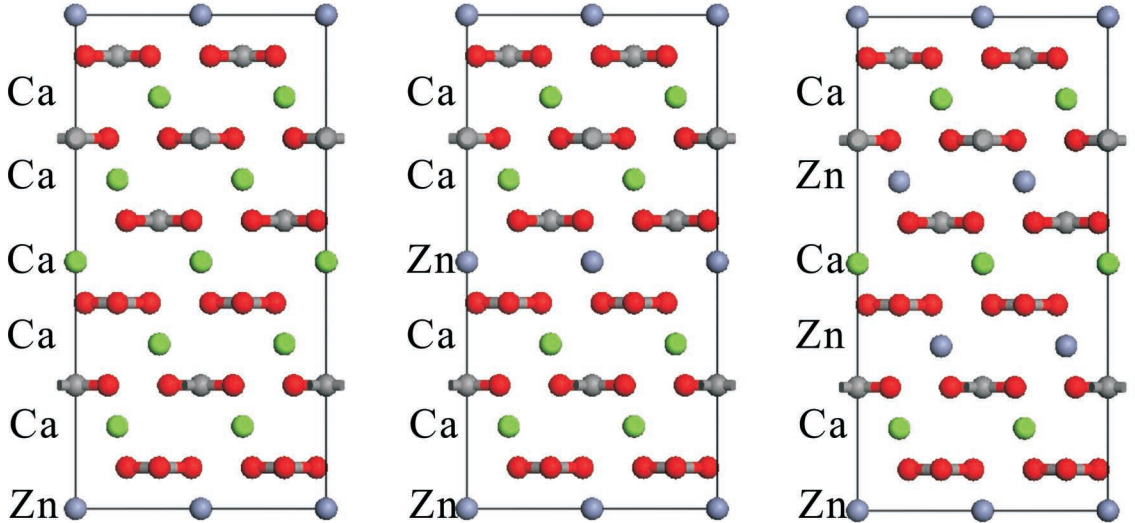
Ca
Ca
Ca
Ca
Ca
Zn
a
Ca
Ca
Zn
Ca
Ca
Zn
b
Ca
Zn
Ca
Zn
Ca
Zn
c

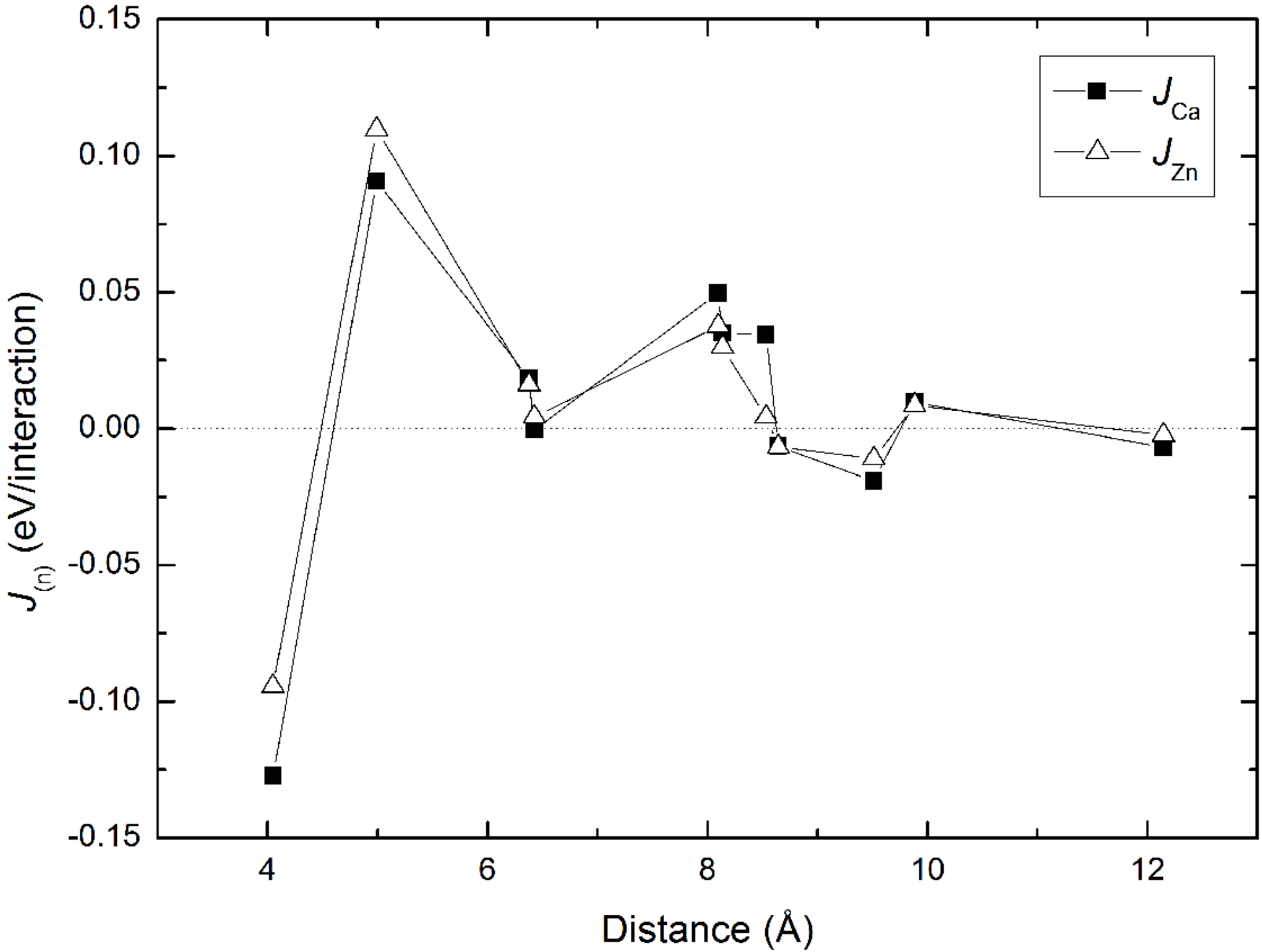
0.15
0.10
0.05
0.00
-0.05
-0.10
-0.15
$J_{(n)}$ (eV/interaction)
4
6
8
10
12
Distance (Å)
J_{Ca}
J_{Zn}

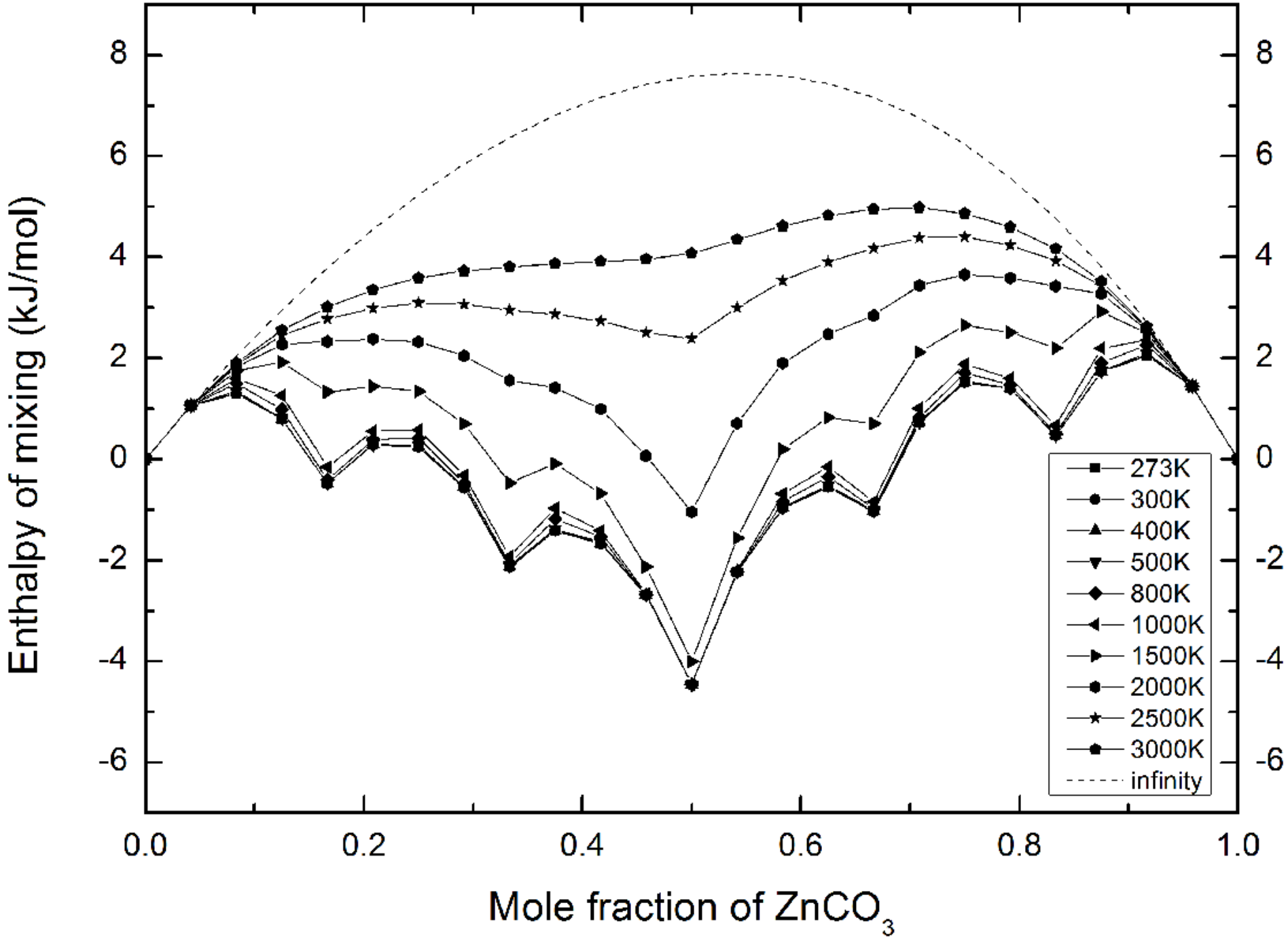
Enthalpy of mixing (kJ/mol)
Mole fraction of ZnCO3
8
6
4
2
0
-2
-4
-6
0.0
0.2
0.4
0.6
0.8
1.0
273K
300K
400K
500K
800K
1000K
1500K
2000K
2500K
3000K
infinity

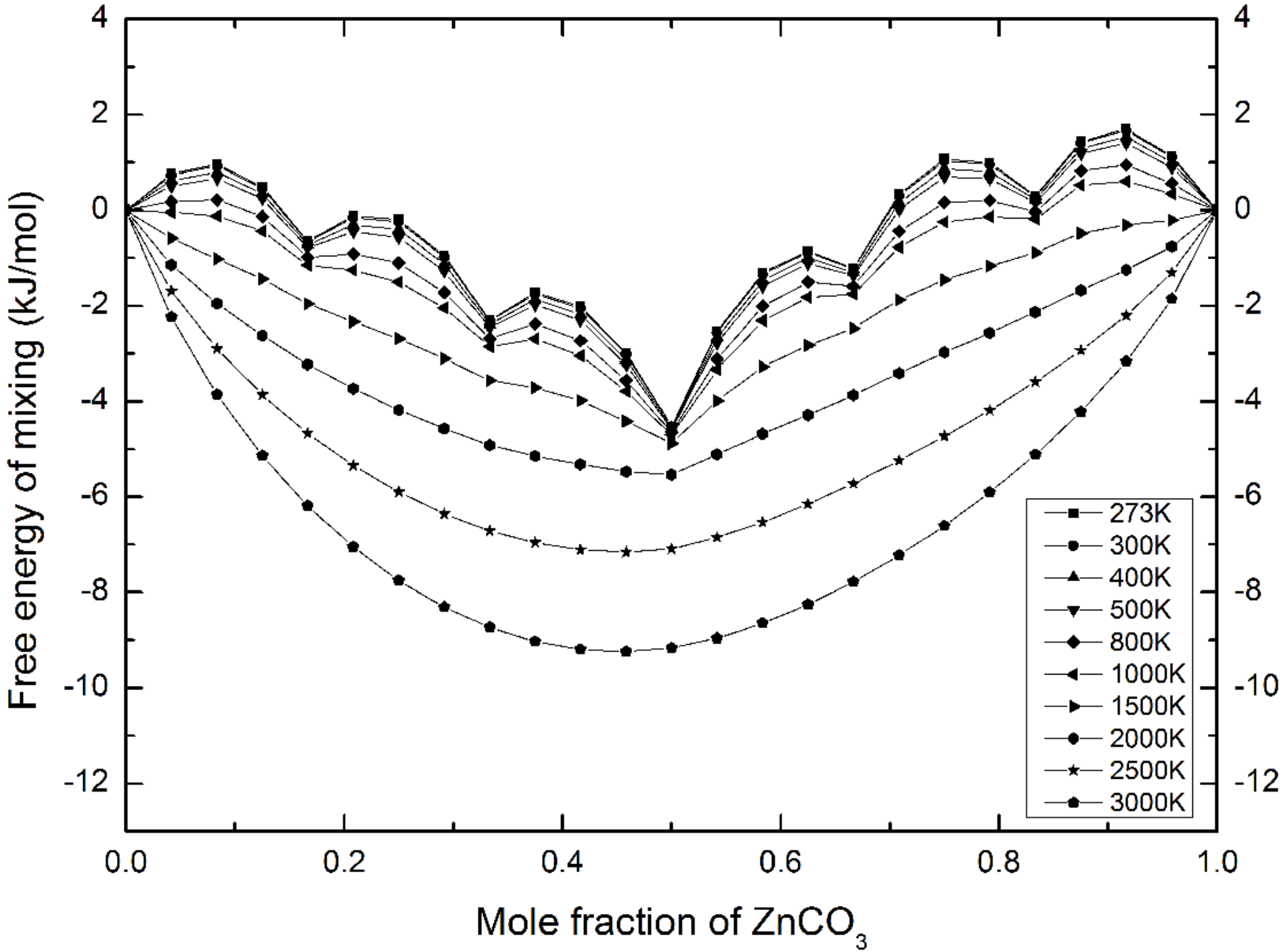
Free energy of mixing (kJ/mol)
Mole fraction of $ZnCO_3$
4
2
0
-2
-4
-6
-8
-10
-12
0.0
0.2
0.4
0.6
0.8
1.0
273K
300K
400K
500K
800K
1000K
1500K
2000K
2500K
3000K

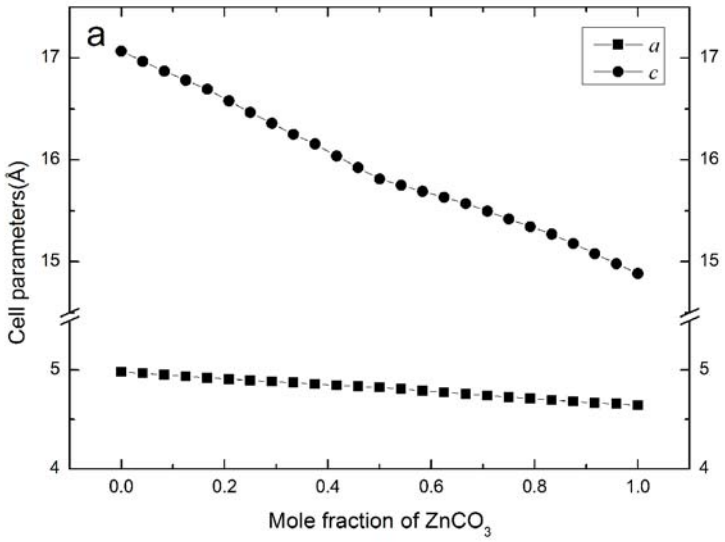
a
a
c
17
16
15
5
4
0.0
0.2
0.4
0.6
0.8
1.0
Cell parameters(Å)
Mole fraction of ZnCO3

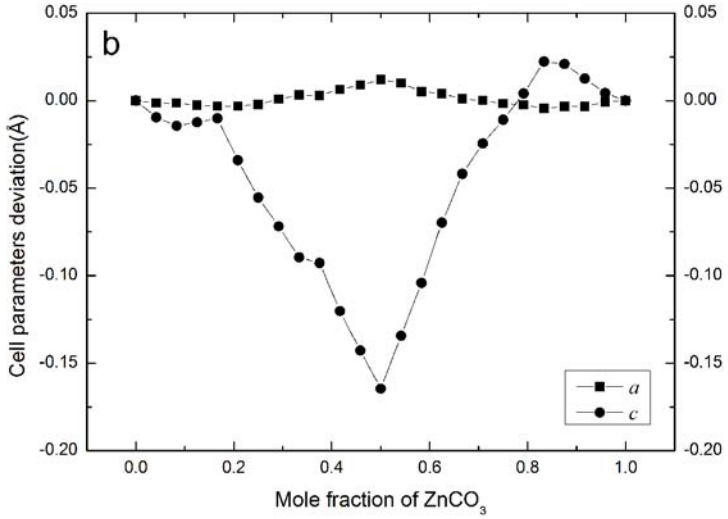
b
Cell parameters deviation(Å)
Mole fraction of ZnCO3
a
c
0.05
0.00
-0.05
-0.10
-0.15
-0.20
0.0
0.2
0.4
0.6
0.8
1.0

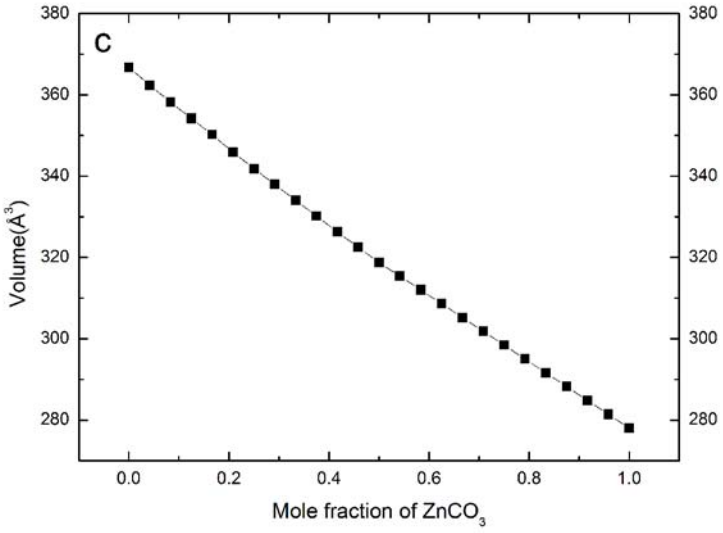
C
Volume(Å^3)
Mole fraction of $ZnCO_3$
380
360
340
320
300
280
0.0
0.2
0.4
0.6
0.8
1.0

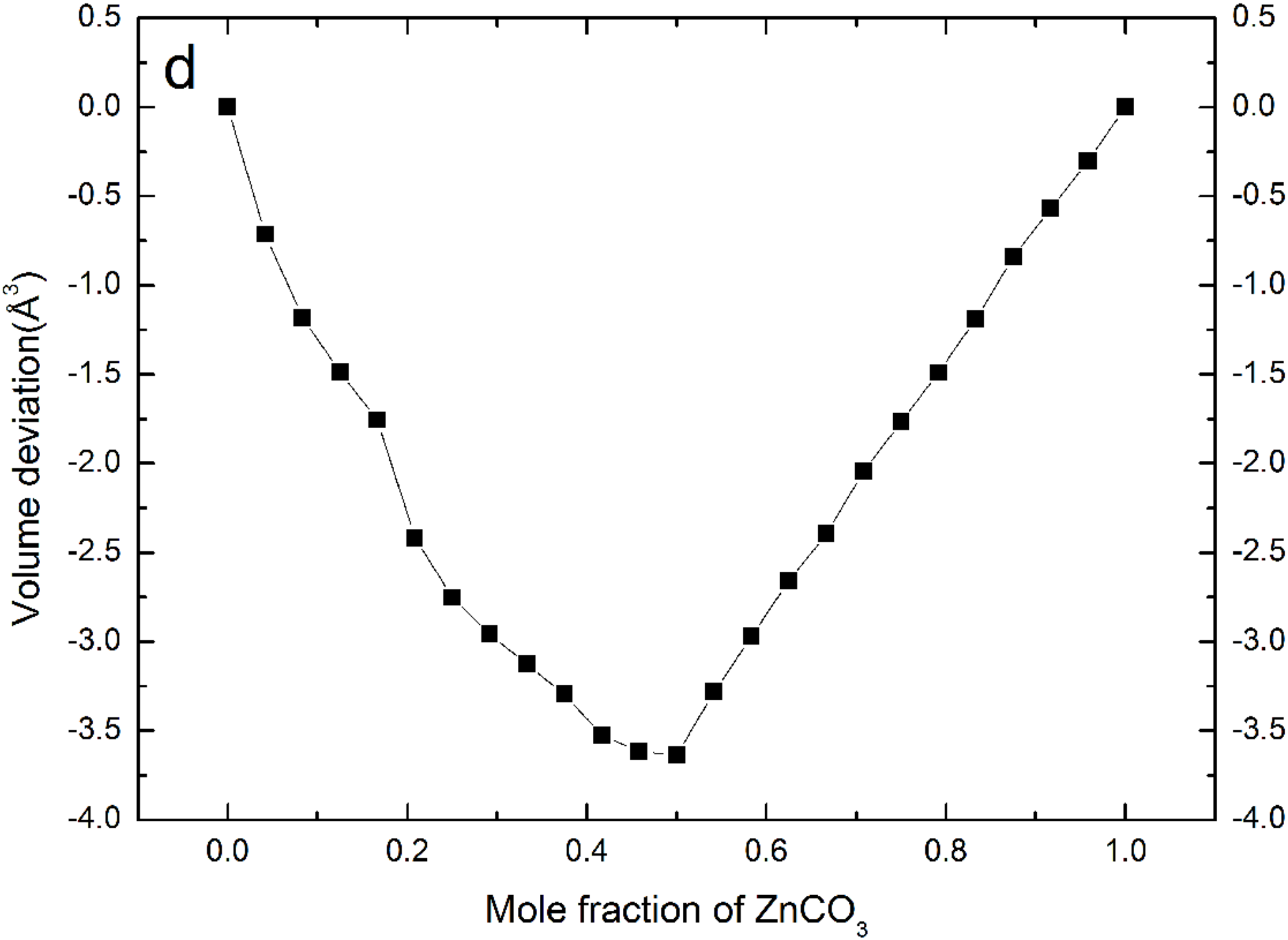
d
0.5
0.0
-0.5
-1.0
-1.5
-2.0
-2.5
-3.0
-3.5
-4.0
Volume deviation(Å^3)
0.0
0.2
0.4
0.6
0.8
1.0
Mole fraction of $ZnCO_3$

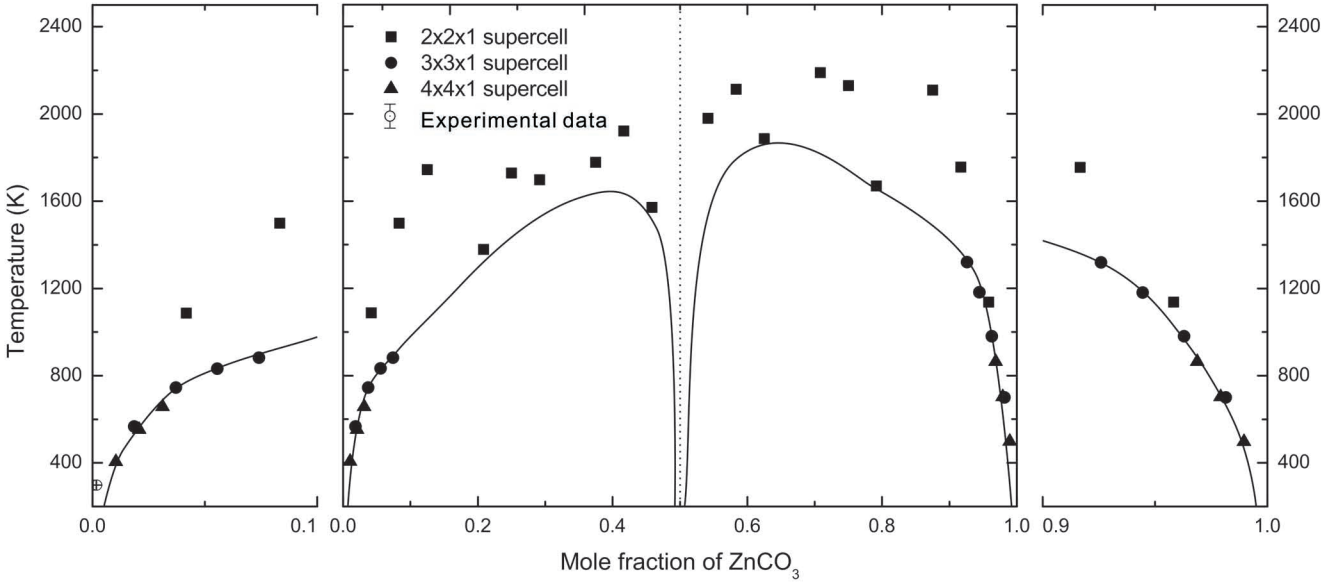
Calcite
Minrecordite
Smithsonite
2x2x1 supercell
3x3x1 supercell
4x4x1 supercell
Experimental data
Temperature (K)
Mole fraction of $ZnCO_3$
2400
2000
1600
1200
800
400
0.0
0.1
0.2
0.4
0.6
0.8
1.0
0.9